IPP-Report

Max-Planck-Institut
für Plasmaphysik

Virgil Alin Popa

Workflow-based energetic particle stability analysis of projected ITER plasmas

IPP 2021-18
Dezember 2021

Max Planck Institute
for Plasma Physics

Technical University of Munich
Department of Physics

Workflow-based energetic particle stability analysis of projected *ITER* plasmas

M.Sc. Thesis in Physics

as part of the group

Max Planck Institute for Plasma Physics

by

Virgil - Alin Popa

Munich, 30/09/2020

Supervisor: Dr. Philipp Lauber

Second Reader: Dr. Stefan Recksiegel

Contents

1 Abstract **1**

2 Introduction and Motivation **3**

2.1 Energy problem 3

2.2 Fusion in the Sun 4

2.3 Fusion in human made devices 5

2.4 Purpose and Structure of this thesis 9

3 Theoretical Description **11**

3.1 Framework 11

3.2 Particle motion in a magnetic field 12

3.3 Wave - particle resonant interaction 13

3.4 Kinetic approach for collective plasma behaviour 15

3.5 Gyrokinetic Theory 16

3.6 Toroidal Alfvén Eigenmodes (TAE) 18

4 Computational Infrastructure and Numerical tools **22**

4.1 Integrated Modelling & Analysis Suite (IMAS) 22

4.2 Energetic Particles Stability Workflow (EP-WF) 22

4.3 HELENA - Equilibrium solver 1 26

4.4 CHEASE - Equilibrium solver 2 27

4.5 LIGKA - Linear Gyrokinetic Solver 27

4.5.1 LIGKA Operating Modes 28

4.5.2 Numerical Implementation of LIGKA 30

5 Local simulations of energetic particle driven modes in ITER (mode 5 and 4) **31**

5.1 Hydrogen Plasma with 1.8T and 5 MA (Time - Dependent) 31

5.1.1 Low toroidal mode numbers 34

5.1.2 High toroidal mode numbers 36
5.2 DT Plasma with 5.3 T and 15 MA (Time-Independent) 36
5.2.1 Low toroidal mode numbers 39
5.2.2 High toroidal mode numbers 40
5.3 DT Plasma with 5.3 T and 10 MA (Time-Independent) 40
5.3.1 Low toroidal mode numbers 43

6 Global simulation of energetic particle driven modes in ITER (mode 5, 4 and 1) 45
6.1 DT Plasma with 5.3T and 15 MA (Time - Dependent) 45
6.1.1 Low toroidal mode numbers 52
6.1.2 High toroidal mode numbers 61

7 Discussion and Summary 64
7.1 Outlook 65

8 Acknowledgements 67

References 68

1 Abstract

Previous analysis show that various Alfvén Eigenmodes (AEs) with different toroidal mode number n and poloidal mode number m can be partially unstable in ITER. Energetic ions, such as fusion born α - particles are moving fast enough that they can resonantly interact with plasma waves such as the Toroidal Alfvén Eigenmode (TAE). Due to the sensitivity of TAEs properties to different profiles, an automated way of analysis is required in order to study their stability. In this work, the first automated time - dependent workflow for energetic particles stability analysis in a fusion plasma was created. The workflow connects the Integrated Modelling Analysis Suite (IMAS) integrated numerical tools (equilibrium code, linear stability code) with the IMAS specific database through Interface Data Structures (IDSs) (see chapter 4). To demonstrate the capabilities of the workflow, 4 scenarios were chosen from the many available in the ITER - IMAS database. Two of them are time - dependent (given by ASTRA (transport code)) and two time - independent (given by METIS (transport code)). An analysis on the frequency and damping of the modes present in this scenario was performed in order to test and validate different parts of the workflow. In chapter 5 local solver (mode 4) was used to find modes present. In a time - dependent pre-fusion plasma scenario from which the overview of the workflow behavior (frequency and damping) was validated for $n = 10, 20, 30$ and multiple m. The first time - independent scenario was studied to check if the deuterium - tritium mix is working properly. With the help of the workflow, the calculation of the damping can be done in an automatic way, in a much shorter time than it has been done before, by hand, in previous papers. The second time - independent scenario was used to check the behaviour of the workflow when a reversed q - profile is present and the implications of this were discussed in chapter 5.3. In chapter 6 the second time - dependent scenario was considered. This scenario is supposed to be the standard for $Q = 10$ ITER baseline DT plasma. Here, the α - particles were also taken into account and a comparison between the local solver (mode 4) and the global solver (mode 1) was performed with and with-

out alpha particles. From this analysis can be seen that no global TAEs are expected to be unstable and the difference between the local and the global solver is mostly seen in damping, where the local model does not take into account radiative damping. Future corrections and implementations are also discussed in the outlook of this thesis.

2 Introduction and Motivation

2.1 Energy problem

All of the world's energy depends on the sun. From fossil fuels to hydropower everything originates ultimately from sunlight. In order to minimize the CO_2 released from burning coal oil or gas world is making efforts to develop solar and wind power but those are presently economically ineffective for the current and future energy consumption worldwide (see fig.1): both solar and wind power are fluctuating (day - night, summer - winter) which makes the energy supplied to the grid unstable. In order to have a stable grid a base-line power supplied is needed. For renewable energy sources this can be achieved through different mechanisms: thermal storage in water, rock or thermochemical systems (for solar power) and gas turbines (for wind power). Fusing atoms together releases nearly four million times more energy than a chemical reaction (burning of coal, oil or gas) and four times as much as nuclear fission reactions. Main advantages are: sustainability (fusion fuels are widely available), no CO_2 emissions, no long-lived radioactive waste, limited risk of proliferation and no risk of meltdown.

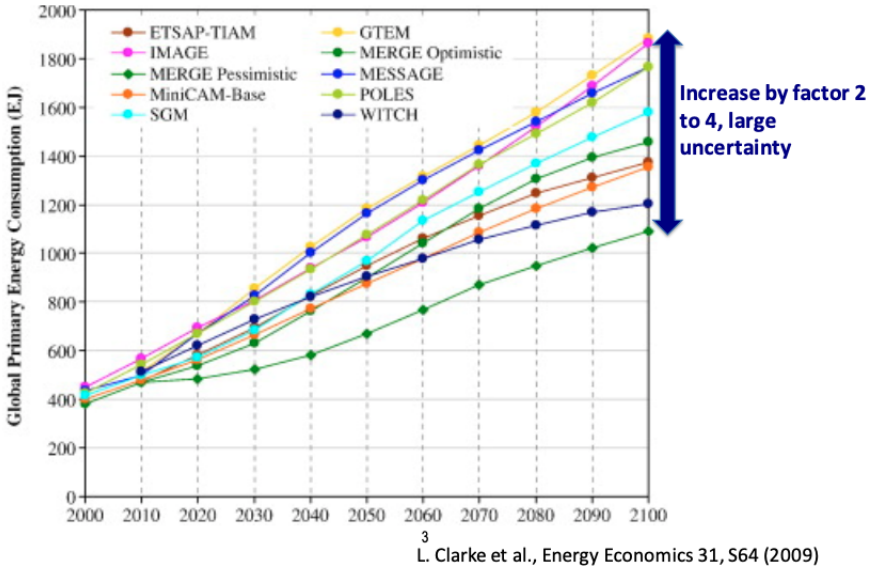

Figure 1: Prediction of energy demand by 2100 performed by different models.

2.2 Fusion in the Sun

The sun's interior has a temperature of about 1 keV. Due to this temperature and the involvement of weak interaction in $4H \rightarrow He^4$, hydrogen atoms live for a million years before they fuse into helium to release energy. Due to the fact that we are unable to recreate the gravitational pool of the sun we need to find other ways to speed up the process. Fortunately, for D + T a resonant He^5 state is accessible by adding only 64 keV to the rest masses energy. One way is to increase the inertia in a head-on collision of heavier isotopes: deuterium (D) with one proton and one neutron, and tritium (T) with one proton and two neutrons. The electrostatic repulsion of the ions needs to be overcame by inertia. Unfortunately we cannot use a particle accelerator to accelerate deutrons and then put a solid piece of tritium ice in the beam. This will not work because the deutrons, due to coulomb scattering, lose more energy in off-angle scatters than they gain in head-on collisions. In fact there is a factor of 100 difference between Coulomb scattering and fusion collisions. There are two main ways to gain energy from a D-T fusion: magnetic confinement and inertial fusion. In this work we will discard the second one and focus on magnetic confinement only.

Magnetic fusion energy (MFE) research has been one of the main research goals of humankind since the mid 20th century. A crucial stage of this research was achieved once the construction of ITER (originally the International Thermonuclear Experimental Reactor) started.[1] In the above mentioned machine, the physics of burning plasmas will be investigated based on a a deuterium-tritium (D-T) fusion reaction:

$$^2D + ^3T \longrightarrow ^4He + ^1n \tag{1}$$

which produces an helium ion (also known as an α particle) with 3.52 MeV and a neutron with 14.06 MeV for a total of 17.58 MeV energy released originating from mass deficit.

The repulsive Coulomb force between the nuclei quickly overrides nuclear attraction at atomic or molecular distances. The kinetic energy of the reactants needs to be large due to the fact that quantum tunneling becomes effective only after a large part of the Coulomb barrier has been penetrated already. As a result, the fusion cross-sections are negligibly small for kinetic energies of less than a few kilo-electron volts (keV). Because the density of fusion reactions depends also on the product of the fusion cross section with particle velocity, the temperature range for which thermonuclear fusion becomes interesting is between $10 - 30$ keV.[2]

There are variants to the deuterium-tritium (D-T) reaction such as the ones presented in Table 1. Even though reactions such as D-D and D-He^3 appear to be a better choice from the economical and environmental point of view (not involving neutrons), with regard to confinement, they are more demanding due to a considerably lower fusion cross-section.

Reactants	**Products**
D - D	T (1 MeV) + p (3 MeV)
D - D	He^3 (0.8 MeV) + n (2.5 MeV)
D - T	He^4 (3.5 MeV) + n (14 MeV)
D - He^3	He^4 (3.7 MeV) + p (14.7 MeV)

Table 1: Fusion reactions with relatively large cross-sections.

2.3 Fusion in human made devices

In fusion reactors , under ideal conditions α particles slow down due to Coulomb collisions with the thermal plasma (thermalize). This ensures the continuous support for the fusion process by keeping $D + T$ at the required temperature. For this reason we have to ensure that the α particles have sufficiently good confinement. Unfortunately, the confinement is far from ideal, and the particle transport properties on timescale τ_p and of plasma energy timescale τ_E must be taken into account. If we neglect the difference between the

two times, the required $n\tau$ in order to breakeven and ignition is shown in Fig.2.

Breakeven occurs when the fusion energy produced is equal to that used in creating the plasma. This is called the Lawson criterion,[3] and the absolute lower limit for the product $n\tau_E$ at $T \simeq 26$ keV is:

$$n\tau_E \gtrapprox 1.5 \cdot 10^{14} cm^{-3} s \tag{2}$$

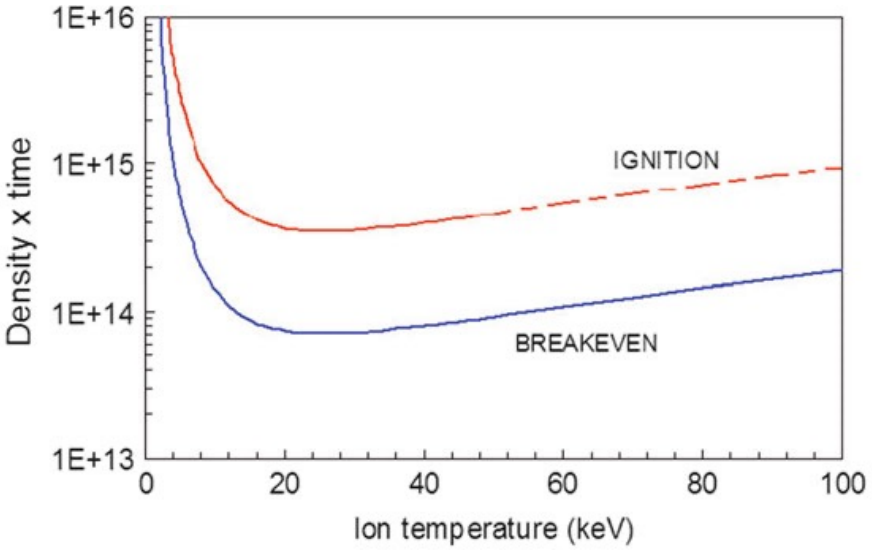

Figure 2: The $n\tau$ product for D-T fusion in units of cm^{-3} s, vs. KT_i[4]

In toroidally symmetric magnetic fusion devices (tokamaks), ITER for example, the geometry of the confining equilibrium magnetic field B_0 properly ensures the confinement of charged-particle orbits, including fusion α particles. A raw schematic of a tokamak can be seen in Fig3. The axisymmetric toroidal device is described by a large magnetic field in the toroidal direction and a smaller poloidal field. Large external field coils produce the toroidal field and the poloidal field is generated by a large toroidal current in the plasma. A transformer with the plasma forming the secondary winding induces the toroidal current mentioned before. Transport due to classical collisional and neoclassical process is sufficiently small and therefore usually small enough to confine α's during their slowing

down time. On the other hand concerns arise in the transport via collective fluctuations driven unstable by α particles via wave-particle resonances. The before mentioned instabilities may be breaking the toroidal symmetry which leads to increased α-particle loss.[5]

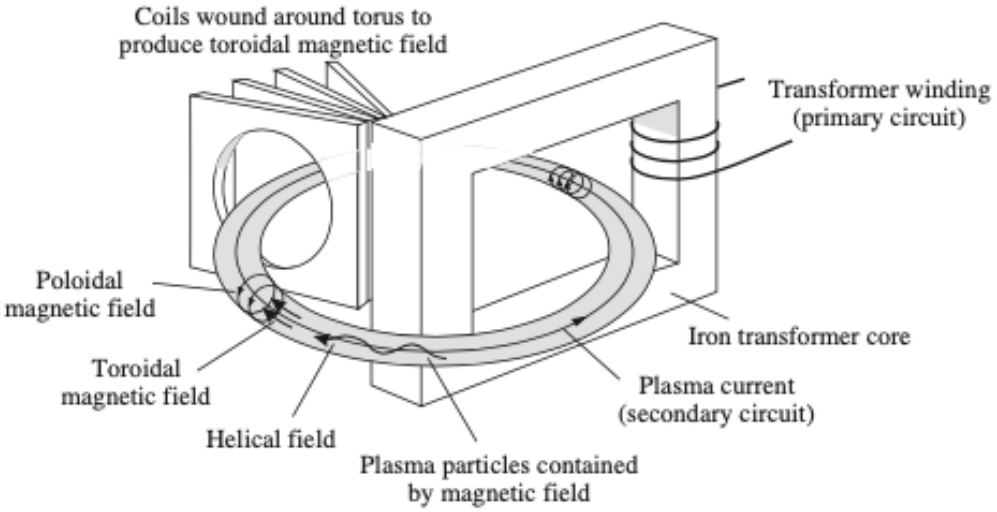

Figure 3: Schematic drawing of a tokamak.[6]

These instabilities can be weakly damped Alfvén waves which resonate with α (suprathermal) particles.[7] For a typical reactor parameters (density $n \sim 10^{20} m^{-3}$, magnetic field $B \sim 6T$) so-called Toroidal Alfvén Eigenmodes (TAE)[8] with phase velocities of the order of the α-particle velocity before thermalization are expected to be the most unstable type of perturbations.[6] Due to the fact that α-particles have a isotropic velocity space distribution function due to the Coulomb collisions the velocity gradient is stabilizing and no collective fluctuations are excited around the cyclotron frequency. But it can be shown that the spatial (radial) gradient can very efficiently provide energy since TAEs tap energy from the radial gradient. Thus, the energy of the TAEs grows and thus flatten the local EPs (αs) gradients (inverse Landau damping).

Because of the high temperature of fast particles (α-particles) which can carry despite their small density $\sim$ 30% of the background pressure some extra considerations are to

be noted:

1. An energetic particle will have a larger gyroradius compared to a thermal particle. This is given by:

$$|q_i| = \frac{|v_{\perp i}|}{\omega_i} \quad \text{with} \quad \omega_i = \frac{Z_i e B}{m_i} \tag{3}$$

where q_i is the gyroradius for a particle of species i with mass m_i and charge $Z_i e$ in a magnetic field B. In Fig.4 can be seen that the gyroradius of helium ion is still small compared to the minor radius of the plasma (2m -ITER) but can become an important factor when compared to the length scales of the MHD modes, e.g. TAEs.[9]

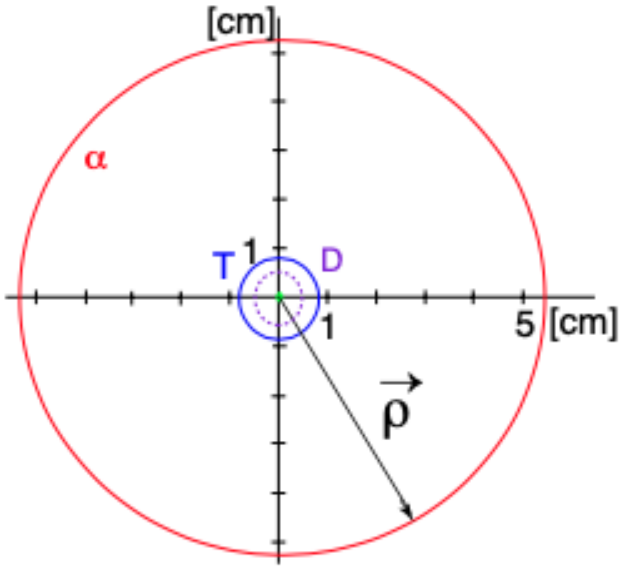

Figure 4: Gyroradii (ITER - $B \sim 5T$) for electrons (0.1mm), deuterium (0.6cm), tritium (0.8cm) and helium (5.3cm) ions.[9]

2. The geometry of the tokamak breaks the rotational geometry of the poloidal coordinate (compared to cylindrical case) and thus adds more innate frequencies to the system, where an effective transfer of energy between the particles and the plasma waves can occur.[9]

Fluid models are not sufficient to capture the relevant effects in energetic particle physics due to kinetic resonances being an essential ingredient (Vlasov equation). Because the Alfvén frequencies are much smaller than cyclotron frequency we can neglect the gyro-motion timescales i.e. $\frac{\omega_{Alfvén}}{\omega_{ci}} << 1$ is ordered out of the system of equations. The relevant perturbations have a spatial structure that is comparable to the Larmor radius and the drift orbit width of the fast (and background) ions. The gyrokinetic equations have been constructed to address this physics. It contains a gyrophase-averaged kinetic equation (particles are treated as drifting charged rings, disregarding the motion of the particle on the ring) that allows for sharp spatial variation of field perturbations on the scale of the ion gyro-radius.

All previous analyses show that many different AEs with different toroidal mode number n and poloidal mode number m can be partially unstable. Due to sensitivity of the Toroidal Alfvén Eigenmodes (TAE) properties to the different profiles an automated way of analysis is required which leads to various α - particle transport models.

2.4 Purpose and Structure of this thesis

In this work the first time-dependent workflow for energetic particles stability analysis in a fusion plasma was created. In the past there were multiple factors that made this hard to achieve: from the difficulty to assess damping, the connection between local-global analysis to the missing of a centralized way of combining the data from various codes under the same structure. These problems were solved once the development of the Integrated Modelling & Analysis Suite (IMAS) done by ITER - Organization,[10] was in an advanced stage and once the codes necessary for different calculations (LIGKA, HELENA) were developed and adapted to work with this new interface.

Here time - dependent means that an automated linear stability analysis is performed for different time points of a projected ITER scenario. These time points are sufficiently separated in time (typically $0.5s - 5s$), i.e. it is assumed that the equilibrium evolution time scale is much longer than the Alfvén time scales connected to the linear and non-linear TAE physics.

A Python time-dependent workflow was created by combining different codes used for analyzing various instabilities in the plasma caused by the energetic particles. In this work, Toroidal Alfvén Eigenmodes (TAE) will be analytically estimated for multiple ITER scenarios with the help of LIGKA (described in the methods chapter)[9] (a Linear Gyrokinetic code). For the data manipulation and storage the Integrated Modelling & Analysis Suite (IMAS) was used and a description of it will be given in the following chapters.

This work is a fundamental and most challenging first step to automated analysis needed for time-dependent cases. Straight forward extensions will lead to various EP transport models.

3 Theoretical Description

In this chapter, the underlying theoretical framework used in this work is introduced and briefly summarized. This is intended as an overview of the theory, not a comprehensive description or demonstration.

3.1 Framework

There are numerous theoretical frameworks that can be used to study energetic particle stability in a tokamak, three of them can be seen in Fig. 5. As mentioned above, kinetic equations are needed for α-physics. In principle, the whole Maxwell - Vlasov system of equations has to be solved in the toroidal geometry. This is very difficult and not practicable due to the complexity of the problem. The system can be simplified in three ways. Either by using the Kinetic Wave Equations, MHD - hybrid models (treating background as a fluid and EPs kinetic) or the framework of Gyrokinetic Theory. In this work, LIGKA

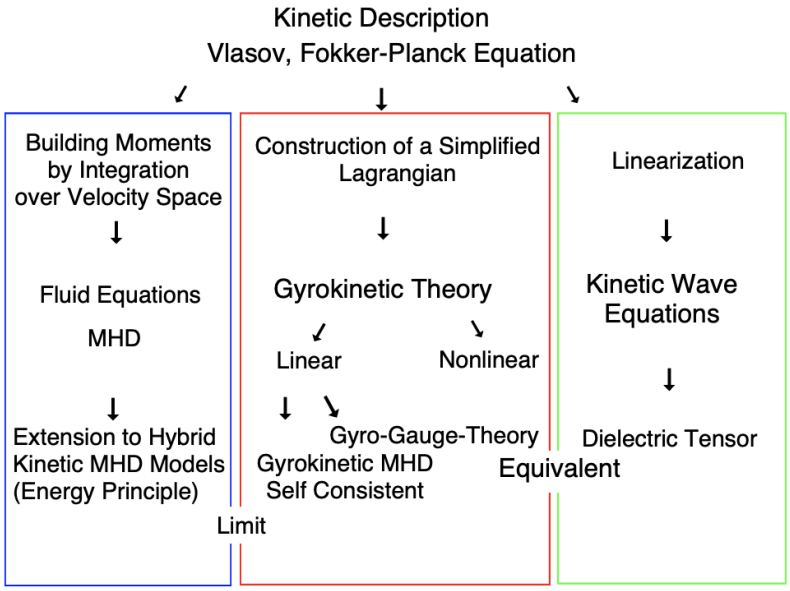

Figure 5: Overview of the branches of kinetic plasma description.[9]

code was used, which makes use of the Gyrokinetic framework. This model consists of three equations: the quasi-neutrality equation (QN), the gyrokinetic moment equation

(GKM) and the gyrokinetic equation (GKE) itself. Electrostatic and electromagnetic potentials, as well as the perturbed distribution functions are the unknowns in the system of equations.[9]

3.2 Particle motion in a magnetic field

Before the Gyrokinetic theory can be explained, a short review and introduction of the basic physics of the plasma is required, namely, the motion of particles in a magnetic field. In the core of a tokamak we have a fully ionized gas trapped inside the structure by strong magnetic fields. Lorentz force is the most important force when it comes to the description of particle orbits in a magnetic field and it is perpendicular to the velocity of the particle and the magnetic field. By neglecting for now the small but fluctuating electric field component we have:

$$\mathbf{F} = q\mathbf{v} \times \mathbf{B} \tag{4}$$

According to the equation, we can see when taking into account only the perpendicular motion, the particle gyrates around a magnetic field line. Gyrofrequency is the frequency associated with such a motion of the particle. The radius associated with this gyration is the Larmor radius:

$$\omega_c = \frac{\mid q \mid B}{m} \qquad \rho_L = \frac{v_\perp}{\omega_c} \tag{5}$$

By taking into account the parallel velocity, we observe that the particle moves freely, parallel to the magnetic field lines. This results in a helical motion of the particle perpendicular to **B**. Drifts are the deviations of the particle motion due to different forces from the helical motion. If we take into account the drift due to a general force **F** we can determine this velocity using the following equation:

$$\mathbf{v}_{drift} = \frac{\mathbf{F} \times \mathbf{B}}{qB^2} \tag{6}$$

we can notice that if **F** will depend on charge q, v_{drift} will not. Otherwise the velocity depends on the charge and will have opposite drifts directions for electrons and ions. In a tokamak, important drifts are: ∇B for which $\mathbf{F} = -\frac{mv_\perp^2}{2qB}\nabla B$ and curvature drifts which has $\mathbf{F} = \frac{mv_\parallel^2}{R_c^2}R_c$.

An important point here is the adiabatic invariant μ, which is proportional to the perpendicular velocity $v_\perp$ and also proportional to $\frac{1}{B}$.

$$\mu = \frac{mv_\perp^2}{2B} \tag{7}$$

This invariant is very important because it causes a fraction of the particles that follow the magnetic field lines to be trapped (mirrored). As a particle moves from a weak-field region to a strong-field region in the course of its thermal motion, it sees an increasing **B**, and therefore $v_\perp$ must increase in order to keep μ constant. Since the total energy of the particle must be conserved, $v_\parallel$ must decrease. If **B** is high enough $v_\parallel$ becomes zero and the particle is "reflected" back to the weak-field region. This effect works on both ions and electrons an is called magnetic mirror trapping.

3.3 Wave - particle resonant interaction

Some energetic particles are moving fast enough that they can resonantly interact with plasma waves such as the Toroidal Alfvén Eigenmode (TAE). This can lead to a transfer of energy from the particles to the wave which in turn can transport the fast particles away from the core of the plasma. Particles can be accelerated or decelerated as a result of the interaction with a wave. A known result of this interaction is Landau damping.[11] We will talk about this process in a one-dimensional system.

Waves have the propagation velocity $v_{phase} = \frac{\omega}{k}$. The net energy transfer strongly depends on the gradient of the distribution function locally around v_{phase}. If a particle moves with $v = v_{phase}$, it will not be accelerated or decelerated by the wave. If $v < v_{phase}$ the particle gains energy from the wave because of the electric field force felt by the particle from the potential of the wave $E(x) = -\nabla\phi(x)$. And finally, if $v > v_{phase}$ we have a transfer of energy from the particle to the wave.

Usually we deal with a Maxwellian distribution in which the gradient of the distribution is negative for all the positive values of v. From Fig.6 we can see that in a Maxwellian distribution there are more slow particles than fast ones, so the overall effect will damp the wave.

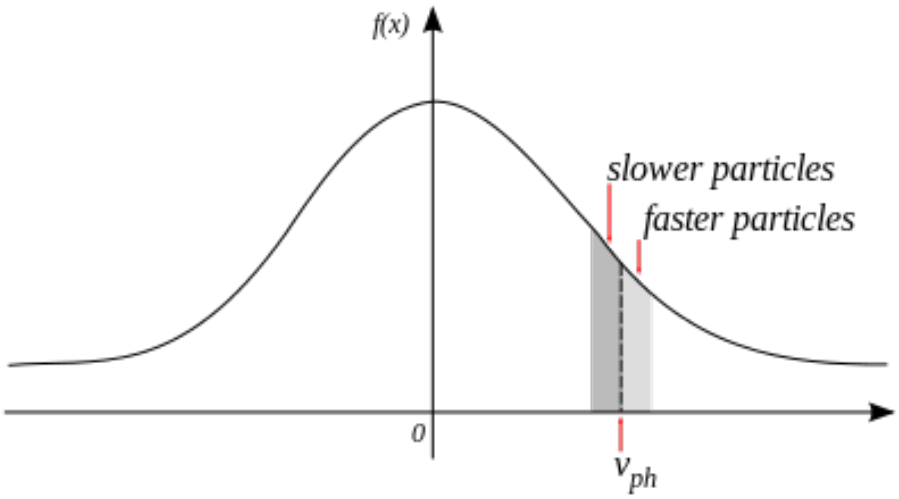

Figure 6: Maxwellian distribution in an ideal plasma.[12]

On the other hand if the distribution is not Maxwellian, see the bump-on-tail distribution in the Figure 7, it can be unstable over a range of wave-numbers. Those waves with phase velocity in positive gradient region would lead to resonant drive of the perturbation and thus lead to a linearly unstable system. In the case of a α - particle distribution, there is no bump-on-tail type of the free available energy of the system, but a radial ener-

getic particle gradient that can act as a source of drive.

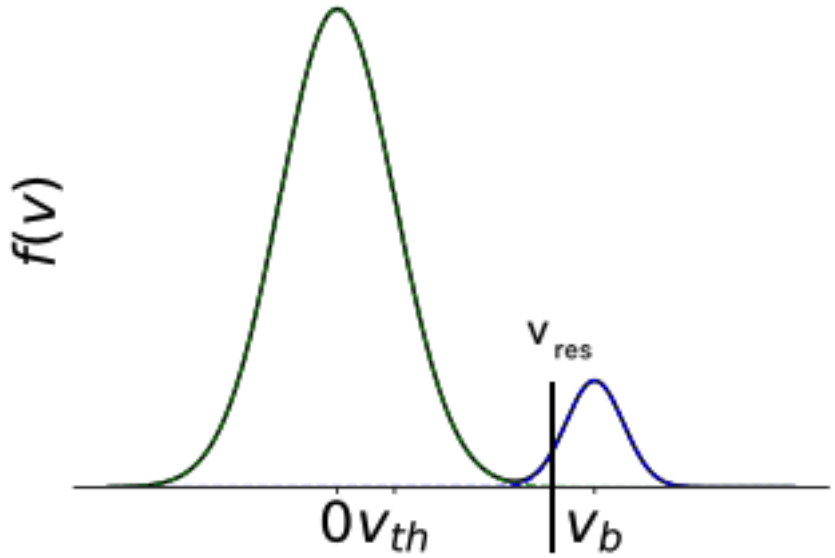

Figure 7: Bump-on-tail distribution, where $v_{res} = \frac{\omega(k)}{k}$ is the resonant velocity of the wave.[13]

3.4 Kinetic approach for collective plasma behaviour

The kinetic theory of a plasma describes the state of a plasma due to its microscopic interactions and motion of its constituents. By considering a fully-ionized, confined plasma we assume that its behaviour can be described by the collisionless non-relativistic Vlasov equation:[14]

$$\frac{\partial f_s}{\partial t} + \mathbf{v} \cdot \nabla f_s + \frac{q_s}{m_s}(\mathbf{E} + \mathbf{v} \times \mathbf{B}) \cdot \frac{\partial f_s}{\partial \mathbf{v}} = 0 \tag{8}$$

This equation describes the evolution of the six-dimensional distribution function phase space of a plasma species s where the right hand side can have a collision operator or sources/sinks added if required. For AEs, typical non-linear timescale is short compared to collisional timescale, this means we can neglect the collision operator.

In order for the description of the system to be complete, Vlasov equation needs to be coupled to the Maxwell equations which describe electromagnetic fields:

$$\nabla \times \mathbf{B} = \mu_0(\mathbf{J} + \epsilon_0 \frac{\partial \mathbf{E}}{\partial t}) \tag{9}$$

$$\nabla \times \mathbf{E} = -\frac{\partial \mathbf{B}}{\partial t} \tag{10}$$

$$\nabla \cdot \mathbf{E} = \frac{\rho}{\epsilon_0} \tag{11}$$

$$\nabla \cdot \mathbf{B} = 0 \tag{12}$$

where ρ is the charge density in the plasma, **J** is the current density and ϵ_0 and μ_0 are the permitivity and permeability of free space. The above equations are also six-dimensional and impractical to solve for fusion plasmas.

3.5 Gyrokinetic Theory

Because of the complexity of the full Vlasov - Maxwell system, a theoretical framework with reduced dimensionality is needed. One of these alternative methods is represented by Gyrokinetic Theory. It takes the Vlasov - Maxwell system of equations in the presence of a magnetic field and transforms the variables in which, by ordering, the gyro-phase is ignored. First, one transforms from particle coordinates (**x**,**v**,t) to guiding-center coordinates ($\mathbf{X}$,$v_{\|}$,$\mathbf{v}_{\perp}$,φ,t). This coordinates are related by:

$$\mathbf{x} = \mathbf{X} + \frac{mc}{q\mathbf{B}} \hat{b} \times \mathbf{v} \tag{13}$$

$$\mathbf{v}_{\perp} = v_{\perp}(\hat{e}_1 cos\varphi - \hat{e}_2 sin\varphi) \tag{14}$$

$$\hat{e}_1 \times \hat{e}_2 = \hat{b} \tag{15}$$

This transformation allows removal of fast gyration from the system and reduction of the dimensionality of phase space from six-dimensional to five-dimensional. This leads to equations in terms of guiding-center i.e. averaging the particle motion around the gyromotion. By taking into account that the perturbations are comparable to the ion ρ_i we can further transform to so-called gyro-centers.

Because of this we can think of particles as moving charge rings instead of point charges. This process yields the gyrokinetic model.[15]

According to reference[16] firstly, we take the linear gyrokinetic quasi-neutrality condition (QNE):

$$0 = \sum_s e_s \int d^2v \{J_0 \delta f\}_s + m_i \nabla_\perp \cdot \frac{n_i \nabla_\perp \delta\phi}{B^2} + \frac{3P_{i\perp}}{4B^2} + \nabla_\perp^4 \delta\phi \tag{16}$$

in which f is the perturbed distribution function, the first term is a sum over all species (ions, fast ions, f, and J_0) and the polarisation terms, which only applies to ions. Next, the linear gyrokinetic momentum equation (GKM) which is the force balance equation:

$$\begin{aligned} -\frac{\partial}{\partial t}\frac{e}{m}\nabla_\perp \frac{n_0}{B^2}\nabla_\perp \phi + \nabla A_\parallel \times \mathbf{b} \cdot \nabla(\frac{\nabla \times \mathbf{B}}{B}) + (\mathbf{B}\cdot\nabla)\frac{(\nabla \times \nabla \times \mathbf{A})\cdot \mathbf{B}}{B^2} \\ = -\sum_a e_a \int \frac{4\pi}{c}\mathbf{v}_d \cdot \nabla J_0 f_a d^3\mathbf{v} + \frac{c}{v_{A0}^2}\frac{3v_{th,a}^2}{4\Omega_a^2}\nabla_\perp^4 \frac{\partial \phi(x)}{\partial t} \\ + \mathbf{B}\cdot\nabla(\frac{4\pi e_a^2 n_{a0} v_{th,a}^2}{2Bm_a c^2 \Omega_a^2}\nabla_\perp^2 A_\parallel) + \mathbf{b}\times\nabla(\frac{2\pi e_a n_{0a} v_{th,a}^2}{B\Omega_a})\cdot\nabla\nabla^2\phi \end{aligned} \tag{17}$$

in which on the LHS we have the inertia term, the parallel equilibrium current term followed by the field line tension and on the RHS the pressure term with the higher order Larmor radius corrections. By separating the perturbed part of the equilibrium part we

can write the linear gyrokinetic equation (GKE):

$$\frac{\partial \delta f_a}{\partial t} + (v_\parallel \mathbf{b} + \mathbf{v}_d) \cdot \nabla \delta f_a = [\frac{\mathbf{b} \times \nabla f_{eq}}{eB} \cdot \nabla - \frac{\partial f_{eq}}{\partial E} \frac{\partial}{\partial t}] \quad J_0 \quad [\delta\phi - (1 - \frac{\mathbf{v}_d \cdot \nabla}{i\omega})\delta\psi] \quad (18)$$

with $\mathbf{v}_d = -\frac{\mathbf{b}}{eB} \times (mv_\parallel^2 (\mathbf{b} \cdot \nabla)\mathbf{b} + \mu \nabla B)$ the drift velocity, ϕ the electrostatic potential, ψ the electromagnetic superpotential ($\partial_t \delta A_\parallel(\mathbf{x}) = -\mathbf{b} \cdot \nabla \delta\psi(\mathbf{x})$) and $J_0 = J_0(\rho k_\perp)$ the gyro-average operator.

In order to solve this system of equations one has to integrate over particle orbits that leads to a the non-linear eigenvalue problem. As a result one obtains eigen-frequencies, growth rate and global mode structure. As input, the equilibrium quantities (such as B, j, P) and the profiles of all species (T,n,F_{EP}) are needed (in this case taken from equilibrium_ids generated by HELENA/CHEASE and core_profiles_ids generated by the transport code METIS or ASTRA) or as measured in the experiment.

It is possible to solve these equations both locally and globally. In general, global analysis is necessary, but local results are often useful and much faster to calculate.

3.6 Toroidal Alfvén Eigenmodes (TAE)

Toroidal Alfvén Eigenmodes (TAE) are the prototype of all Alfvénic Eigenmodes (AE).[17] They have a frequency inside the shear Alfvén continuum gap and their mode structure is given by the coupling of two counterpropagating regular shear Alfvén waves. TAEs can be excited through resonance by fast particles and fusion products because their parallel group velocity in toroidal devices is typically of the same order as parallel particle speed. These modes are dangerous for particle transport because the perpendicular group velocity can be neglected and thus, the resonant condition can be maintained effectively.

The shear Alfvén wave dispersion relation in a cylinder is:

$$\omega^2 = k_n^2 v_A^2 = (\frac{nq-m}{qR})^2 v_A^2 = (\frac{nq-m}{qR})^2 \frac{B^2}{n_i m_i \mu_0} \tag{19}$$

where the ions density, n_i - profile determine the solution with $\omega^2 \sim \frac{1}{n}$. In cylinder, the dashed lines from Fig.8 left side we can see that the solutions for different m, $m+1$ can cross. In a tokamak, the same figure shows that the crossing is replaced by gaps due to toroidal corrections of $\sum_m \omega^2 = k_m^2 v_A^2$.

The poloidal coupling is due to the periodicity of the magnetic field in poloidal coordinates. This leads to the existence of a gap between the two continua.

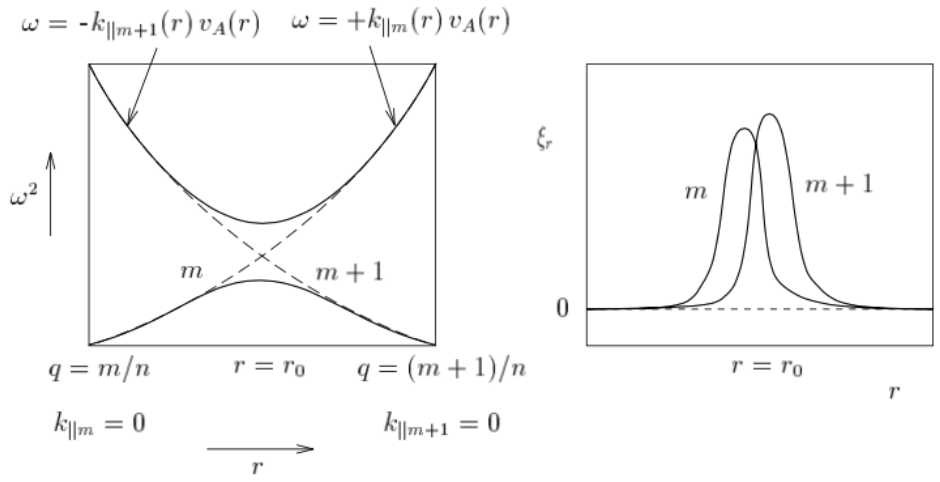

Figure 8: Coupling of poloidal harmonics in a torus and the corresponding TAE eigenfunctions.[6]

The two 'bands' correspond to a localization of the wave in either the 'good' curvature or the 'bad' one. The radial localization of the gap is determined by:

$$k_{\|m}(r_0) + k_{\|m+1}(r_0) = 0 \tag{20}$$

This is equivalent to the position where:

$$q(r_0) = \frac{m+\frac{1}{2}}{n} \tag{21}$$

with the width of the gap being described by:

$$\Delta_{AE} \cong \frac{r_0}{m} \tag{22}$$

Investigating radially localized regions of TAEs gaps taking into consideration various toroidal (n) and poloidal (m) mode numbers requires a closer look at the $q(r)$ - profile.

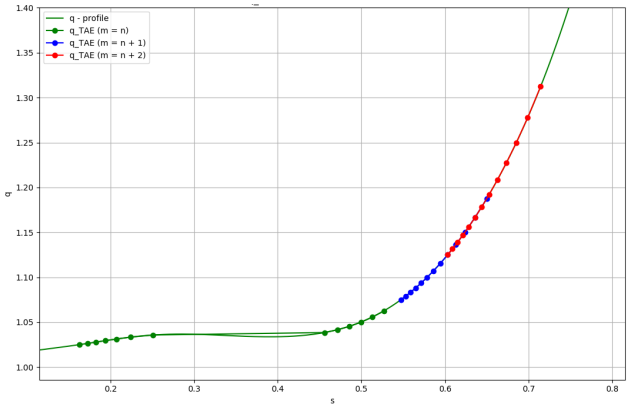

Figure 9: The safety factor (q - profile) and the rational surfaces $q(s_{TAE})$ of $m = n, n+1, n+2$ for different n

According to[18] the characteristic frequency of TAE in toroidal plasmas with $q^2\bar{\beta} \ll 1$ is calculated according to the formula:

$$\omega_{TAE} = \frac{1}{2q} \frac{\mid 2 - \sqrt{1 + \frac{3\epsilon_{g2}^2}{4}} \mid}{\sqrt{1 - \frac{\epsilon_{g2}^2}{4}}} \tag{23}$$

where $\bar{\beta} = \frac{\beta_s}{1+\beta_s}$ and $\beta_s = \frac{c_s^2}{v_A^2}$ for high q, which is characteristic for the core region of the tokamaks, and $\epsilon_{g2} = \frac{k^2-1}{k^2+1}$ describing higher order geometry effects (plasma elongation).

The dispersion relation describing the coupling of the ideal MHD TAE with a kinetic Alfvén wave is:

$$\omega = \pm k_{\parallel} m v_A [1 + (\frac{3}{4} + \frac{T_e}{T_i})(k_{\perp}\rho_i)^2] \tag{24}$$

The effect known as the 'radiative damping' of TAE is the mechanism that drives the energy away from the localisation of TAE eigenfunction in form of outgoing radiative kinetic Alfvén wave (KAW).[19] In addition, there is ion and electron Landau damping. In order to obtain instability, the drive from the α - particles has to overcome the sum of all damping.

4 Computational Infrastructure and Numerical tools

In order to study the Physics of Toroidal Alfvén Eigenmodes (TAE) in time-dependent and time-independent scenarios we need to use a Database in/from which we can put/take the data in a consistent way (IMAS[10]), a full workflow which manages all the numerical tools and the manipulation of data sets (Energetic Particle Stability workflow) and last but not least the numerical models required to perform the simulations (HELENA[20]/CHEASE[21] and LIGKA[9]). In this section all of them will be discussed with focus on the role that they had in this work.

4.1 Integrated Modelling & Analysis Suite (IMAS)

The ITER Integrated Modeling and Analysis Suite was developed for the purpose of meeting the needs of the ITER project. Namely, for an accurate prediction of fusion performance and developing efficient control techniques which support the preparation for ITER operation and exploitation phase. The infrastructure consists of an standardised data model capable of describing both experimental and simulated data using the same representation for both. It consists of Interface Data Structures (IDSs) that have the purpose of facilitating the data exchange between different physics components, as well as making the data visualization and analysis easier. Along with the datasets that are very specific in IMAS, there is also an ensemble of software management tools to support the integration and development of physics components such as tools to automate building and regression testing prior to release.

4.2 Energetic Particles Stability Workflow (EP-WF)

In order to be able to connect the numerical tools with IMAS and to be able to perform time-dependent analysis on any scenario, Energetic Particle Stability Workflow was created. This is the first time-dependent workflow which uses IMAS infrastructure to

perform Energetic particle analysis. It is written in Python and makes use also of a simple interface which makes parameter configuration easy for both the connection to the IMAS Database (for saving/retrieving data) and for the numerical codes themselves through a series of XML files. A general layout of the components that the workflow uses can be seen in Fig.10.

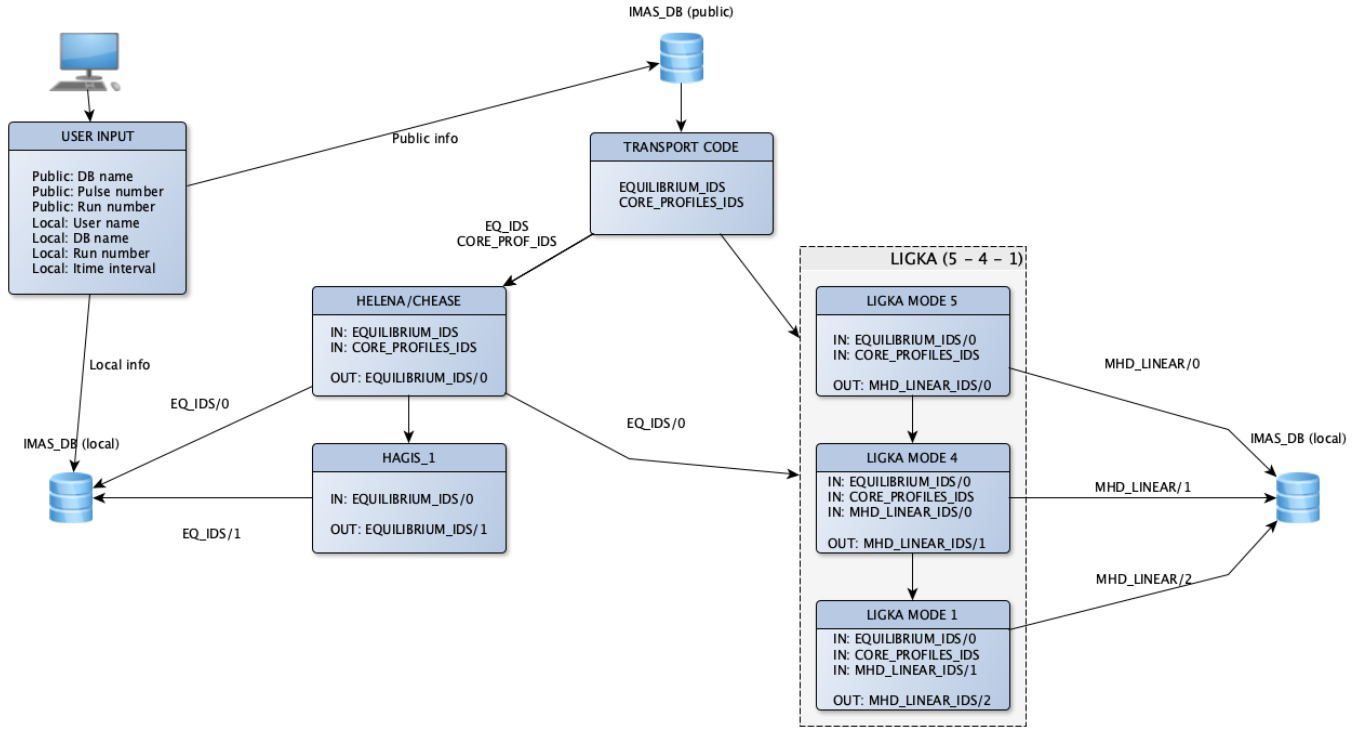

Figure 10: Energetic Particle Stability Workflow general layout of the components.

As can be seen in the figure above, the user has to select as inputs the database from which he takes the information (either public or local one), the shot number, the run number and the time interval that he wants to run the workflow on. As outputs, the user selects the database name and the run number, the convection in IMAS about shot number is that it remains the same as for the input. Each numerical tool can be called separately, provided that the necessary information is in the selected database. For the purpose of explaining the capabilities of the workflow, we will select the full 'ligka - 541' option. This branch of the workflow consists of taking the data and applying various

numerical tools to it directly from the transport database, until 'mode 1' of LIGKA. The steps that are being followed here are:

1. Takes equilibrium_ids from the transport code, initially in the public database and passes it into HELENA/CHEASE (both do similar transformations and give the same result, it is up to the user to choose whichever is more convenient). The equilibrium code gives as an output equilibrium_ids/0 at high resolution (*/0 means occurrence 0, one can have many instances of the same IDS in one workflow). The output is saved in the local database for reference/later usage).

2. Together with equilibrium_ids/0, core_profiles_ids is being taken from the transport code and given as inputs for Mode 5 of LIGKA. This and all LIGKA modes will be described in the next subsections. Mode 5 performs analytical estimates of TAE (and other AEs) and creates as an output mhd_linear_ids/0 which in turn it is being saved in the local database.

3. Next is mode 4 of LIGKA which takes as an input equilibrium_ids/0, core_profiles_ids/0 and mhd_linear_ids/0 and creates a new occurrence of the mhd_linear_ids/1. This part represents the local solver.

4. Finally, mode 1 of LIGKA is being used and as a necessary input IDSs we have: equilibrium_ids/0, core_profiles_ids/0 and mhd_linear_ids/1 (output from mode 4) and also creates a new occurrence of mhd_linear_ids/2. In this part a global solver is used.

This workflow is also equipped to work with other numerical tools such as HAGIS 1 and 2 for non-linear stability of EPs, but this surpasses the scope of this thesis. Because it is structured in computational blocks, it can be adapted to run almost any numerical tool in connection with IMAS. Due to this, reproducibility of results is possible.

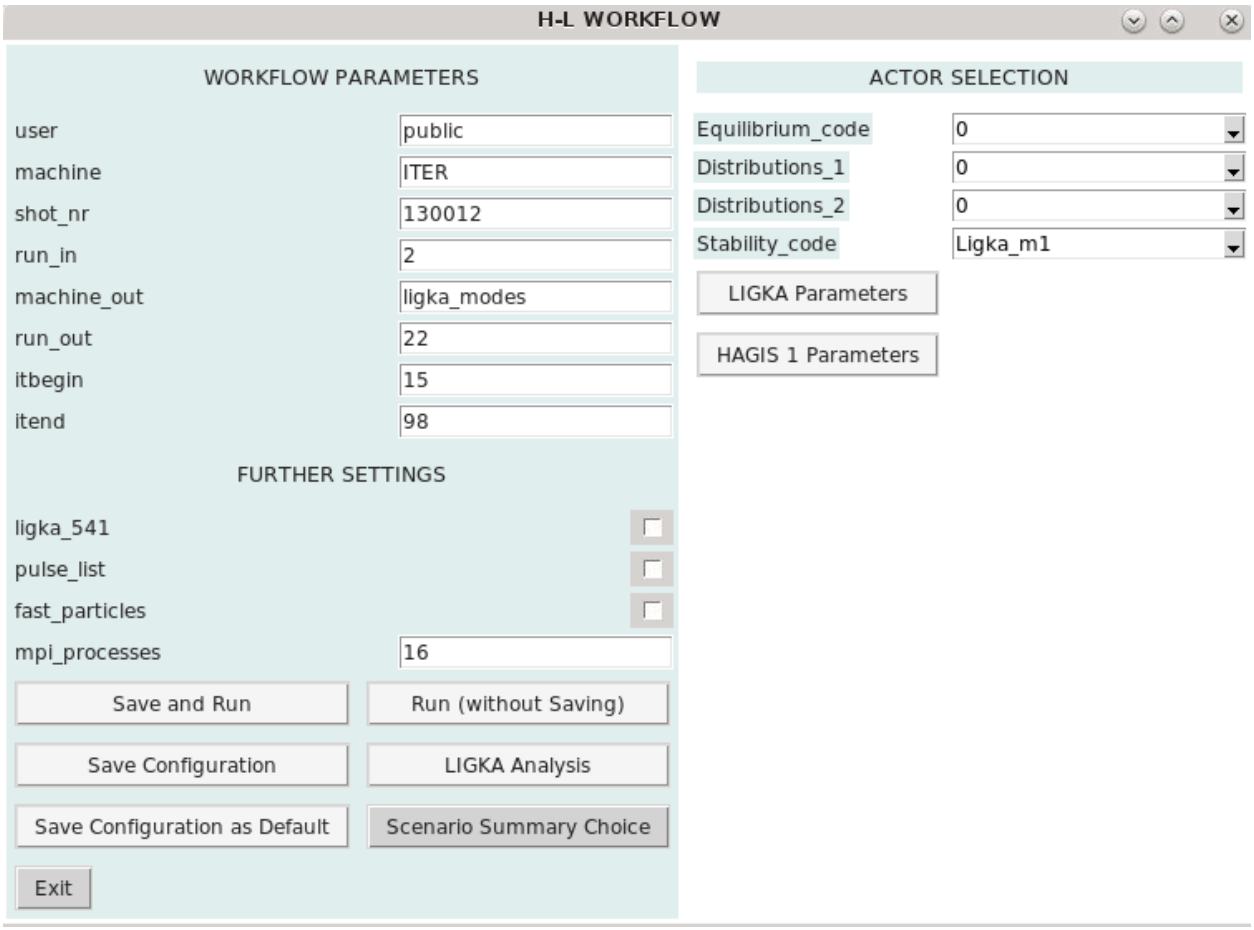

Figure 11: Energetic Particle Stability Workflow User Interface.

In Fig.11 a snapshot of the user interface can be seen. On the left side under "WORKFLOW PARAMETERS" the general settings related to the reading from the database such as user, machine, shot_nr, run_in and itbegin (first time-point) and itend (end time-point) as well as the setting to where to save the newly created IDSs (machine_out, run_out). In "FURTHER SETTINGS" extra features of the workflow can be found, such as the option to run the whole workflow with 1 click (HELENA + LIGKA mode5 , mode 4 and mode 1), pulse_list which allows multiple shots to be run with the same settings without having the need of reconfiguration, fast_particles tells the workflow to modify the LIGKA XML accordingly and to include fast particles in the run. LIGKA is a MPI code and such the mpi_processes determines the number of processes to be used when running the code. On the right side of the user interface, "ACTOR SELECTION" is the place where once can

select a single code to be used (given that all the prerequisites are fulfilled). Under this section the buttons to modify the XML parameters of LIGKA and HAGIS 1 can be found. A large part of LIGKA's parameters are configured automatically by the workflow such as the plasma composition (read and configured from the core_profiles_IDS).

The first iteration of the program was made using Kepler (2019) because of the lack of support for Python at that time inside the IMAS low level infrastructure. Kepler, like IMASPy later, worked with blocks of code called actors and each of them had to be called sequentially and interconnected one with another. The main problem with this was integrating different codes to read and write IDSs (see chapter 4). This was a lengthy process from the moment this project started until the time this work was written because of the constant development of the IMAS data structures. A continuous adaptation and improvement needed to be done on the workflow itself due to the development of IMASPy (addition/removal of new/deprecated routines). At the same time, the development and usage of the EP-Stability WF has helped to speed up the process of developing and fixing IMASPy. The aim of the program written for this work is to collect the features/options from all actors under a single program so they can be used together faster and easier. All data in this thesis that was simulated/post-processed and plotted was done via the workflow.

4.3 HELENA - Equilibrium solver 1

HELENA is a computer code written in Fortran 77 that solves the MHD equilibrium equation of a toroidal axisymmetric plasma. This is done by solving the Grad-Shafranov equation for the poloidal flux ψ(R,Z).

$$\Delta^* \psi \equiv R \frac{\partial}{\partial R}\left(\frac{1}{R}\frac{\partial \psi}{\partial R}\right) + \frac{\partial^2 \psi}{\partial Z^2} = \mu_0 R J_\phi \tag{25}$$

$$\mu_0 R J_\phi = -\mu_0 R^2 \frac{dP(\psi)}{d\psi} - \frac{1}{2}\frac{dF^2(\psi)}{d\psi} \tag{26}$$

where J_ϕ is the toroidal current density, R is the distance from the axis of symmetry and Z is the vertical coordinate.[20]

In this workflow, HELENA/CHEASE has to be run first because we need a MHD equilibrium for the input in LIGKA in sufficiently high resolution.

4.4 CHEASE - Equilibrium solver 2

A more flexible alternative to HELENA is the Cubic Hermite Element Axisymmetric Static Equilibrium[21] (CHEASE). This code solves the same equation as HELENA does. What makes it more viable for our case is it's ability to automatically generate new pressure profiles marginally stable to ballooning modes or given a prescribed fraction of bootstrap current. Because of this, one can use different q profiles to compare them and test LIGKA in different scenarios without constructing a whole new transport simulation. Also this code is more versatile by being able to provide equilibrium quantities necessary for a wide range of stability codes. It was shown that the codes agree almost perfectly for most of the selected cases.

4.5 LIGKA - Linear Gyrokinetic Solver

The workflow and this whole thesis is centered around the Linear Gyrokinetic Shear Alfven Physics (LIGKA) code. This is a model which solves the linearized gyrokinetic equations to find the eigenvalues and eigenfunctions of the system i.e. frequency, damping and mode structure (see chapter 3.6 above).

Due to symmetry present in a tokamak, the toroidal modes are decoupled because of toroidal symmetry and can be treated separately. In contrast, for the poloidal angle they are coupled and such we have coupled m's. As described in[9] a system of coupled

differential equations in radial direction for ϕ with complex eigenvalue ω is obtained. This equations are then solved with finite element method.

In the following the different operation modes of LIGKA are described as well as a general numerical implementation of the code.

4.5.1 LIGKA Operating Modes

1. Mode 5: Based on the profiles given in equilibrium_ids/0 (HELENA/CHEASE output) and core_profiles_ids/0 (from transport code) analytical estimates[18 22] for various basic properties of AEs are calculated and stored in mhd_linear_ids (frequency, estimated mode structure, damping rate, rational surface, next and previous gap information, etc.). The type of modes that are currently being investigated (TAE, RSAE, BAE, EAE (not explained here, other types of SAW in addition to TAE)) is chosen via code_params as given in the Python actor (agreed naming of the adapted numerical code for IMAS-Python interface). Other inputs are: range of toroidal and poloidal mode numbers, odd/even parity, number of radial grid points for output, number and type of ion species. A complete description of all parameters can be found in a commented XML/XSD file which can be directly modified from the EP-WF interface (gui, see chapter 4.2). Mode 5 is almost instant, the runtime is typically below 1s (this is for one time slice, and without taking into account the time to load the data from the different IDSs). This mode is central to the workflow, because all other modes require mode 5 output, so this mode has to be run first before all other modes.

2. Mode 4: Based on the results of mode 5 the local analytical dispersion relation for one mode (n,m-pair) is calculated.[23] Should there be more modes in the mhd_linear_ids/0 IDS all modes are processed in the same order as they are stored in the IDS. Output

are the complex frequency of the maximum or minimum of the continuum closest to the modes rational surface, giving a good estimate for ion Landau damping and local electron Landau damping. This information is crucial to determine the starting point for global (antenna-type) calculations, i.e. scan through the gap region on order to find all possible modes close to the mode5-defined (rational) surface.

3. Mode 3: same as mode 4, but use Finite Larmor Radius (FLR)/Finite Orbit Width (FOW) dispersion relation in order to obtain an estimate for radiative damping.[24]

4. Mode 1: Based on the results of mode 4 (or 3), perform a frequency scan throughout the gap or close to local extremum (BAE, RSAE) in order to find global linear properties of modes, i.e. the location of the the gobal mode in the gap. Depending on the input parameter kin_mode either analytical estimates or HAGIS pre-calculated coefficients for the kinetic orbit integrals are used. Also a mixed choice (analytical for ions and electrons, numerical for fast ions) is possible. Typically, more than one mode is found. All found modes (damping <10%) are stored in mhd_linear_ids/2.

5. Mode 2: The same as mode 1, but in mode 2 just one mode is tracked, such that a more accurate growth/damping rate can be obtained or the runtime can be reduced by starting the scan close to the modes frequency as determined by mode 1.

6. Mode 6: Use a reduced MHD model to calculate all eigenvalues and eigenvectors in the reduced MHD limit. This solver is not parallelised yet, so it becomes very slow for large matrices. Also memory becomes an issue for high resolution with a large m-spectrum. Therefore, it is recommended to use this mode with 128 radial points with m_max-m_min< 30. Write out one gobal mode with mode peak close to mode 5 defined rational surface into mhd_linear_3. Also the ideal MHD continuum is provided. This mode is used for benchmarks only since the physics is inherently kinetic.

4.5.2 Numerical Implementation of LIGKA

LIGKA is made to work in correlation with other codes described in previous sections. In the workflow around which this paper is written LIGKA represents the endpoint of the calculations per time-step. The structure of the code itself is a follows:[9]

1. Reading in the equilibrium from HELENA.
2. Computing coefficients from the differential operators of the GKM equation.
3. By employing Galerkin's method algebraic equations are being set up.
4. Kinetic data is being read.
5. An eigenvalue is being guessed, evaluation of the velocity space integrals and adding the results to the coefficients of the differential equations.
6. Solve global matrix for guess.
7. Repeating step 5 and 6 until a converged solution is found.

5 Local simulations of energetic particle driven modes in ITER (mode 5 and 4)

For the purpose of demonstrating the capabilities of the newly developed workflow, as well as tuning of the analytical estimates given by Mode 5 (and later mode 4) in LIGKA 4 scenarios were chosen from the many available in the ITER - IMAS database. Two of them are time-dependent and two time-independent. For time-dependent scenario the output of METIS[25] (a fast integrated tokamak modelling tool for scenario design) will be used and for the time-independent scenarios the one from ASTRA[26] (Automatic System for TRansport Analysis). For the purpose of demonstrating the capabilities of both LIGKA and the new workflow that it is integrated in, the focus will be on Toroidal Alfvén Eigenmodes structure and effects on the plasma stability, such as growth/damping rate of the perturbation. Because of the workflow automation, we can simulate different scenarios for an extended range of toroidal mode numbers at the same time (high n and low n). We will look at the different behaviours for each case and discuss the underlying physics.

5.1 Hydrogen Plasma with 1.8T and 5 MA (Time - Dependent)

In this first time-dependent scenario, we consider a pre-Fusion Hydrogen plasma. This represents the first operation phase in ITER. During this phase, no α - particles are present. However, a small amount of energetic ions is provided by Neutral beam heating, that also virtually can destabilize TAEs. Based on the results from this phase, ITER operation will be tested and pioneered. Plasma composition can be seen in Table 2, deduced from the core_profiles_ids generated by METIS. Other parameters of this scenario, can be viewed in Table 3. In this scenario, the evolution of the plasma is counter from 1.5 seconds to 647 seconds in steps of 3.71 seconds. That means 175 time-steps. With mode 5 (analytical mode) of LIGKA 145 time-steps were calculated. Because of the increased complexity of mode 4 calculations, only 17 time-steps out of those were selected. This predictive

scenario can be found under shot number 100015, run number 1 in ITER Database.

Species:	H	D	T	He3	Be	W
A:	1.0	2.0	3.0	3.0	9.0	183.0
Z:	1.0	1.0	1.0	2.0	4.0	74.0
n_over_ntot:	0.973	9.82e-03	3.93e-20	3.93e-20	0.017	1.55e-06
n_over_ne:	0.925	9.34e-03	3.74e-20	3.74e-20	0.017	1.47e-06
n_over_n_maj:	1.000	0.010	4.04e-20	4.04e-20	0.018	1.59e-06

Table 2: Plasma composition deducted from the IDS.

confinement_regime:	L-H-L
magnetic_field:	-1.8 [T]
main_species:	H
plasma_current:	-5.00 [MA]
central_electron_density:	4.47e+19 [m^{-3}]

Table 3: Scenario properties.

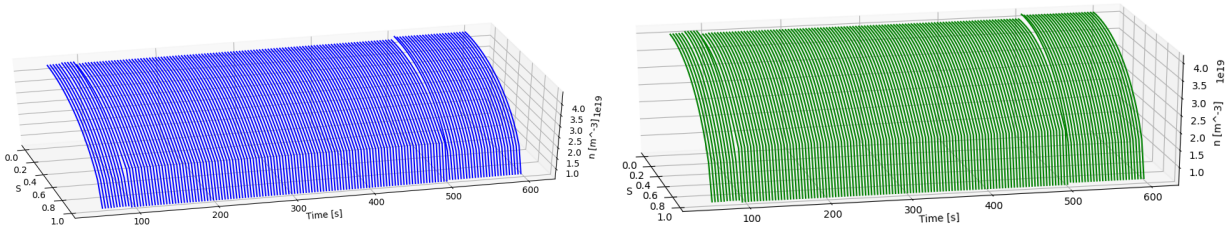

(a) (b)

Figure 12: Time evolution of a) The electron density profile, b) The ions (H) density profile.

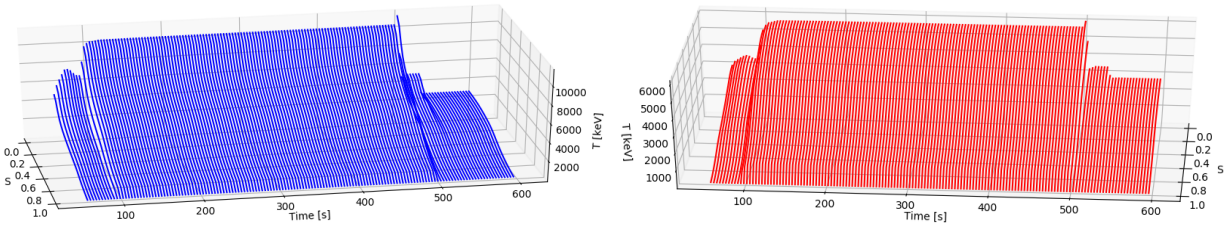

(a) (b)

Figure 13: Time evolution of a) The electron temperature profile, b) The ions (H) temperature profile.

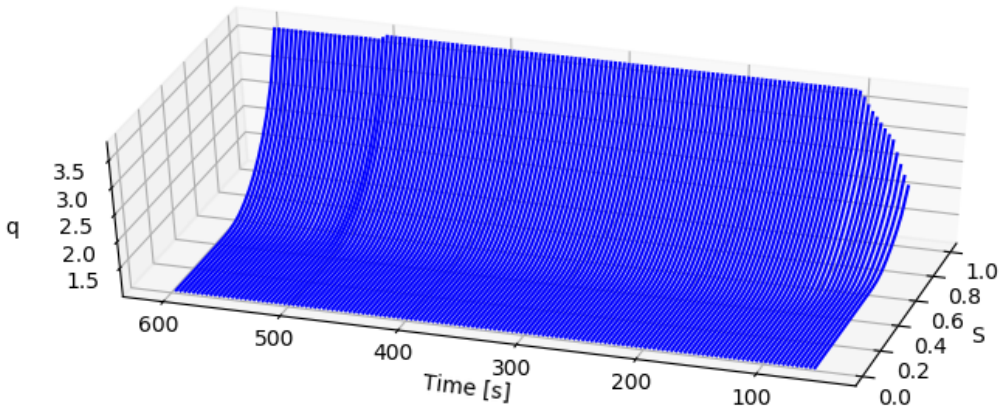

Figure 14: The safety factor (q - profile).

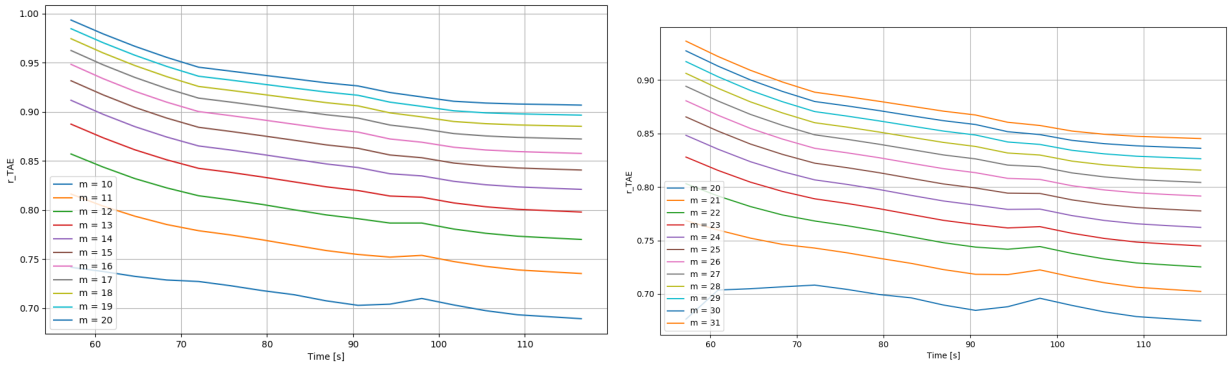

(a) (b)

Figure 15: Time evolution of a) the radial position of TAEs $n = 10$ for different m, b) the radial position of TAEs $n = 20$ for different m.

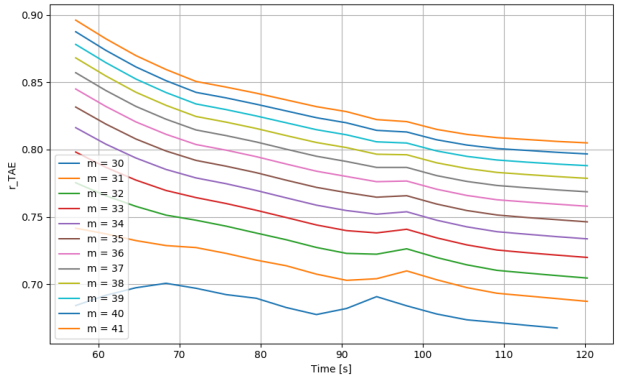

Figure 16: Time evolution of the radial position of TAEs $n = 30$ for different m.

In Figure 15 and 16 the time evolution of the radial positions of TAEs for $n = 10, 20, 30$ is plotted as given by the local solver in LIGKA (mode 4). As expected, modes with higher

poloidal mode number m compared to the toroidal mode number, n, are going one by one towards the edge of the plasma as m increases. For the purpose of a stability analysis, usually the modes with high m compared to n ($m > n + 5$) so the modes that are towards the edge of the plasma will not be taken into account, because they are very localized and the do not get much drive from the fast particles (fast particle density gradient is very much higher at mid radius of the reactor than at the edge, in this case we do not have fast particles taken into account).

5.1.1 Low toroidal mode numbers

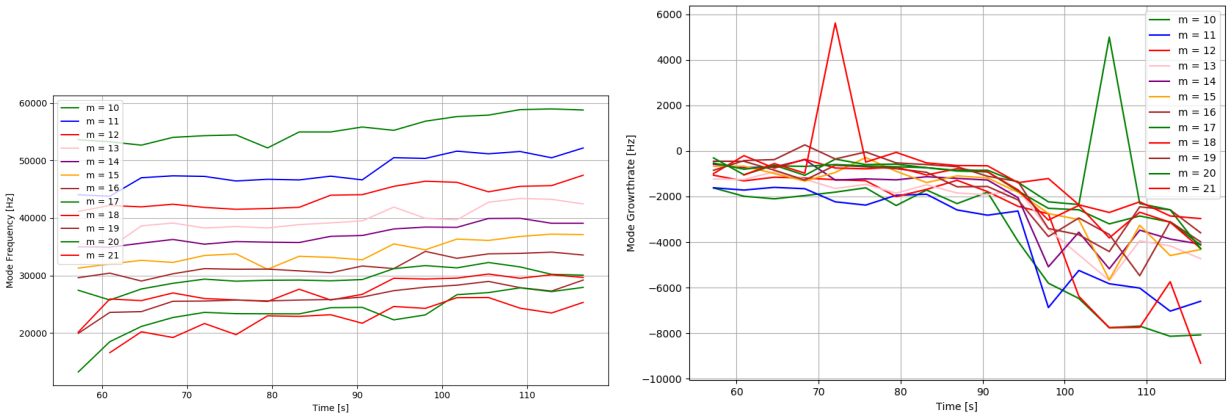

(a) (b)

Figure 17: Time evolution of a) TAE frequency found for $n = 10$ for different m without considering alpha particles. b) TAE growth/damping for $n = 10$ with no alpha particles present.

In order to get a overview of how the workflow behaves, here, more than 5 poloidal mode numbers were taken into account for each n. In Figure 17 (a) the time evolution of frequencies of the modes found with $n = 10$ are plotted and it can be seen that the frequencies are dropping with increasing m. This supports the fact that the only modes one needs to be concerned about are the ones that have $m = n, n + 1, n + 2, n + 3$. An important mention in regarding TAEs is that even though they have 2 harmonics, each with a different poloidal mode number, as a reference point we mention only the lowest harmonic i.e the lowest poloidal mode number m. In figure (b) the time evolution of

the damping for each m is plotted. As expected, due to the ion Landau damping the damping is increasing as we go from the ramp-up phase ($t = 57s - 80s$) to the flat-top phase ($t = 80s-$). One can observe two abnormalities in this graph, for $m = 21$ at $t = 75s$ and $m = 20$ at $t = 105s$. These jumps are due to the algorithm that calculates local damping , which is still not perfect, so at large shear and non-sufficient radial resolution (256 points now). Again, for the large m ($m > 15$) the modes are not of interest due to their radial location, which is close to the edge (explained above).

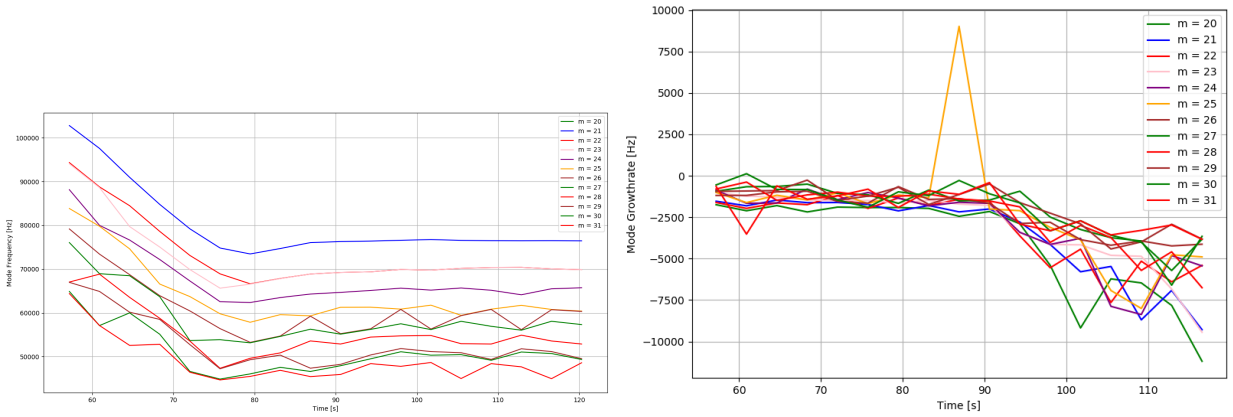

(a) (b)

Figure 18: Time evolution of a) TAE frequency found for $n = 20$ for different m without considering alpha particles. b) TAE growth/damping for $n = 20$ with no alpha particles present.

In figure 18 we can see the same quantities, this time for $n = 20$ and again, a large spectrum of poloidal mode numbers m. In (a) the ramp-up phase and flat-top is very visible in frequency with higher values for the ramp-up and then lower for the flat-top. Again, the lower m modes have higher frequency than the low m. In (b) the trend is the same as for the $n = 10$ and this time the abnormality is present in $m = 25$ for $t = 88s$ and a smaller deviation in $m = 31$ for $t = 61s$. These modes can be discarded from a future global analysis (mode 1) because they have high m in comparison to n (see argument above).

5.1.2 High toroidal mode numbers

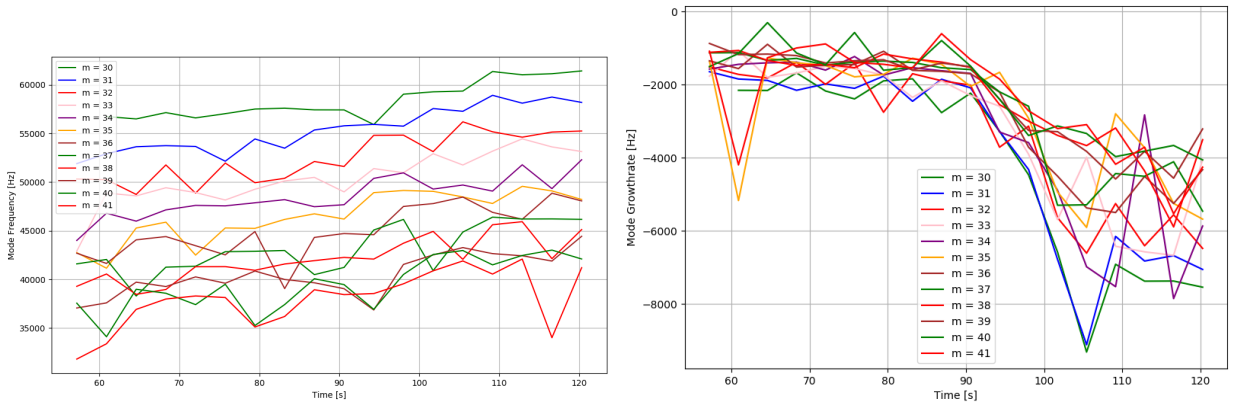

(a) (b)

Figure 19: Time evolution of a) TAE frequency found for $n = 30$ for different m without considering alpha particles. b) TAE growth/damping for $n = 30$ with no alpha particles present.

In figure 19 the time evolution of frequency and damping for $n = 30$ with different poloidal mode numbers are plotted. In the frequency the same behaviour as for $n = 10$ can be noticed, the frequency depends strongly on the radial position of the modes by comparing with figure 16. Again, for the damping the effect of temperature can be noticed after $t = 80s$ when the temperature increases, the damping also increases due to the increased electron and ion Landau damping. Abnormalities can be found again at the beginning of (b) $t = 61s$ again, for high poloidal mode numbers compared to toroidal mode numbers. These modes are not of interest for a stability analysis as explained before.

5.2 DT Plasma with 5.3 T and 15 MA (Time-Independent)

In this first time - independent scenario generated by ASTRA, the fuelling is made up from Deuterium - Tritium. It is a predictive scenario, with only one time-point at 208s. Thus, the runs are performed on the whole simulation, rather than just the selected parts like in the time-dependent cases. The composition of the plasma can be viewed in Table 4. Compared to the other scenarios, here we can also see that the main species of the ASTRA

output include He^4. That means that the density of the species is bigger than in previous scenarios, and such, the contribution to the Energetic Particle physics must be bigger. The properties of the scenario such as, confinement regime, magnetic field strength, main species and plasma current can be seen in Table 5. This predictive scenario can be found under shot number 131025, run number 20 in ITER Database and it is very close to the baseline scenario studied before in several papers.[27 28 13]

Species:	D	T	He3	He4	H	Be	Ne	W
A:	2.0e+00	3.0e+00	3.0e+00	4.0e+00	1.0e+00	8.0e+00	2.0e+0	1.8e+02
Z:	1.0e+00	1.0e+00	2.0e+00	2.0e+00	1.0e+00	4.0e+00	1.0e+01	7.4e+01
n_over_ntot:	4.6e-01	4.6e-01	6.3e-05	5.7e-02	6.1e-05	2.3e-02	2.3e-03	1.1e-05
n_over_ne:	4.0e-01	4.0e-01	5.5e-05	5.0e-02	5.3e-05	2.0e-02	2.0e-03	1.0e-05
n_over_n_maj:	9.9e-01	1.0e+00	1.4e-04	1.2e-01	1.3e-04	5.0e-02	5.0e-03	2.5e-05

Table 4: Plasma composition deducted from the IDS.

confinement_regime:	H-Mode
magnetic_field:	-5.30 [T]
main_species:	D-T-He4
plasma_current:	-15.00 [MA]
central_electron_density:	1.18e+20 [m^{-3}]

Table 5: Scenario properties.

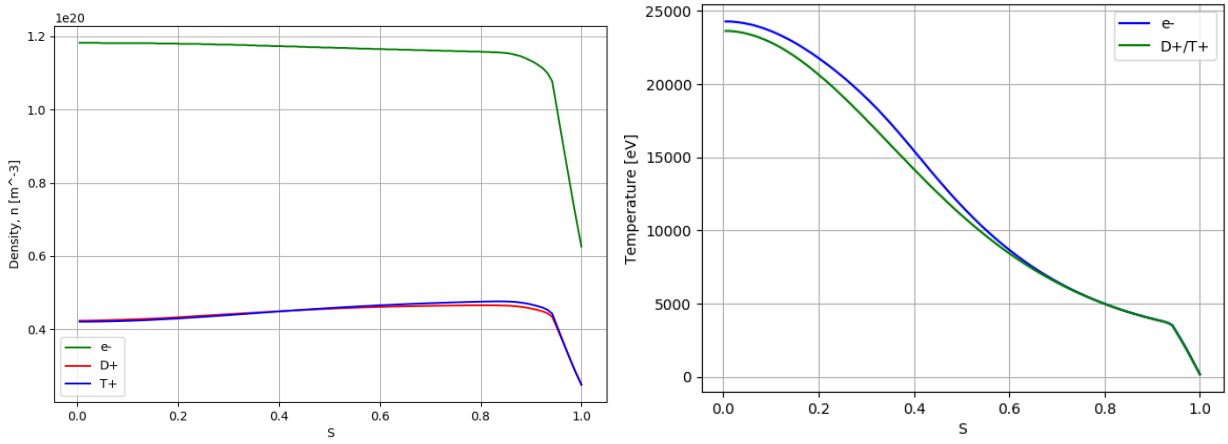

(a) (b)

Figure 20: a) The electron, Deuterium and Tritium density profile, b) The electron and Deuterium/Tritium temperature profile.

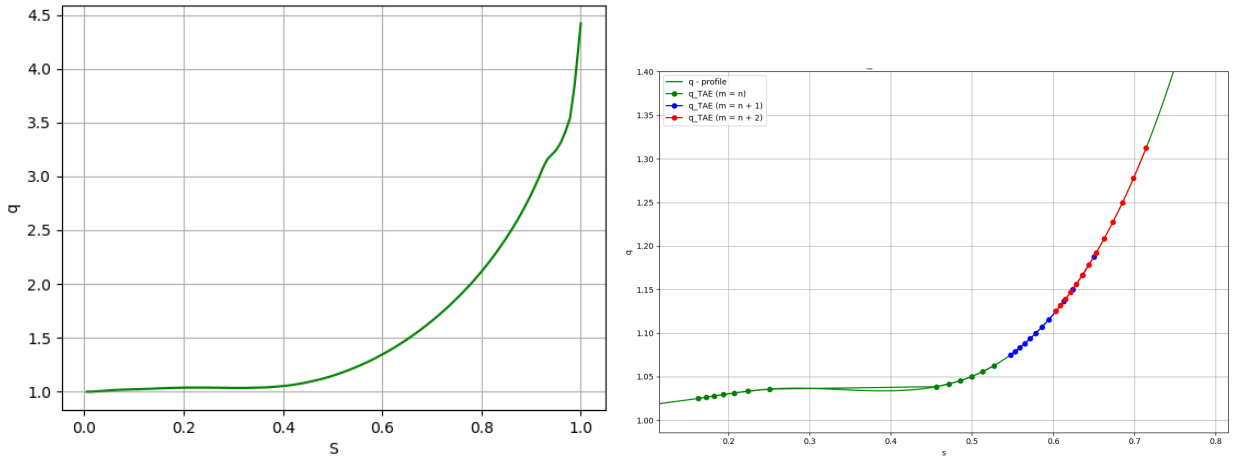

(a) (b)

Figure 21: a) The safety factor (q - profile), b) The safety factor (q - profile) and the rational surfaces q(s_TAE) of $m = n, n + 1, n + 2$ for different n.

In chapter 5.1, a pre-fusion plasma was analyzed, here we also have Neutral Beam Heating (NBI), this is not yet added to the workflow. In this chapter we are interested in the damping of the modes, without any alpha particles taken into consideration. α - particles will be considered in more detail in chapter 6. This is done to check if the deuterium - tritium mix is working properly (the multi-species part of the workflow). In figure 21 both the q - profile and the q values at the radial locations of TAEs are plotted for different toroidal mode numbers and $m = n, n + 1, n + 2$. A filter has been applied for the modes in graph (b), the position of the TAE needs to be larger than 0.3. It can be seen that the $m = n$ modes have values that are under $r_{TAE} < 0.4$, this will reflect in both the frequency and damping of the modes, in the next part.

5.2.1 Low toroidal mode numbers

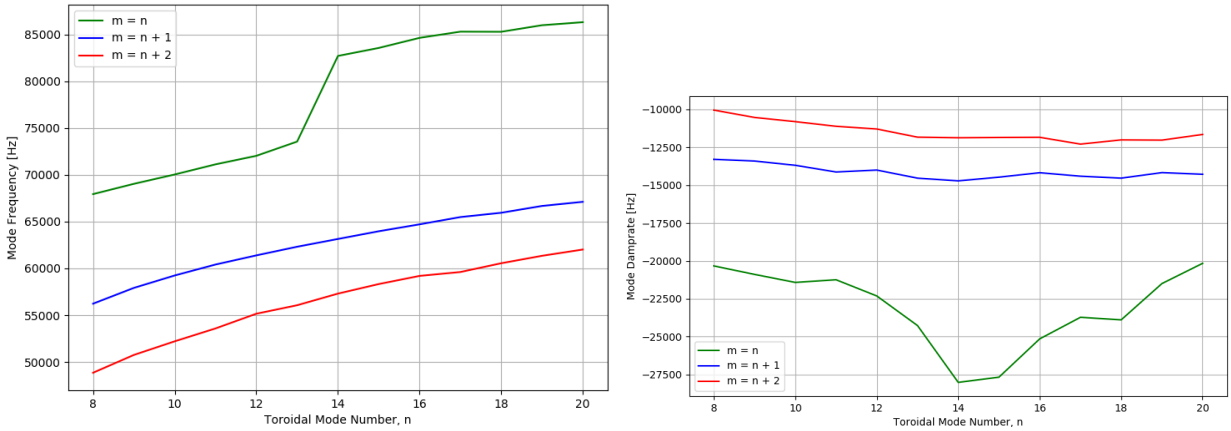

(a) (b)

Figure 22: a) Mode Frequency vs Toroidal Mode Number for 3 different poloidal mode numbers b) Damping vs Toroidal Mode Number for 3 different poloidal mode numbers.

In figure 22 the frequency (a) and the damping (b) were plotted as a function of the toroidal mode number for 3 different $m = n, n+1, n+2$. Again, it is clear that the frequency increases with decreasing m and also increases with increasing n. For the frequency a jump can be observed for $n = 13, 14$ at $m = n$. This is due to the fact that the q - profile is not monotonic and thus, the modes are part of another TAE root. This can be seen in figure 21(b), the green line (q_{TAE} for $m = n$) has a point that has a radial position further away than the rest ($r_{TAE} < 0.4$). This point is precisely the point where the jump happens, and after that the graph continues on that trend with the rest of the remaining toroidal mode numbers having a higher frequency than before the jump. For the damping (b), we can see the same effect, when the jump in the frequency happens, the damping is increased and then, once the $m = n$ modes are continuing on the normal trend, the damping goes back to $-20000\frac{1}{s}$.

5.2.2 High toroidal mode numbers

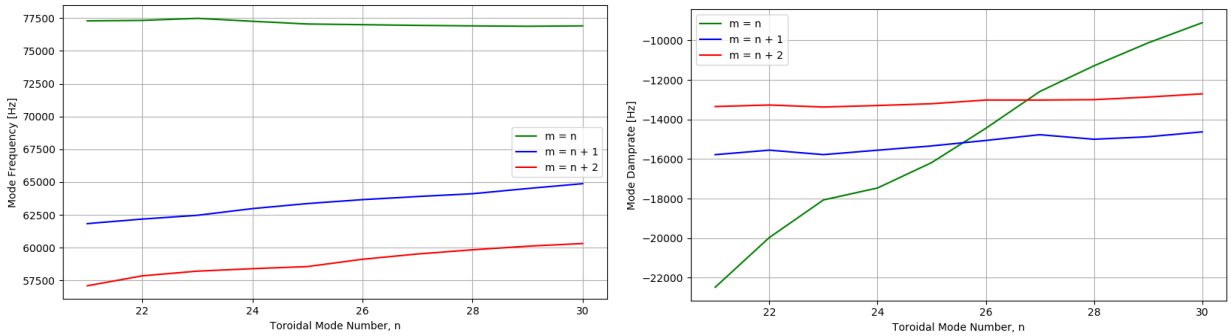

(a) (b)

Figure 23: a) Mode Frequency vs Toroidal Mode Number for 3 different poloidal mode numbers b) Damping vs Toroidal Mode Number for 3 different poloidal mode numbers.

As shown in previous analysis of this scenario, the modes that are the most unstable are the ones with the toroidal mode numbers between $n = 20, 30$. With the help of the workflow, the calculation of the damping can be done in an automatic way, in a much shorter time than it has been done before, by hand, in previous papers.

5.3 DT Plasma with 5.3 T and 10 MA (Time-Independent)

In the second time-independent scenario we have a smaller plasma current compared to the previous time-independent case, namely 10 MA. The fuelling is made out of Deuterium - Tritium and again, the analysis can be performed over the entire scenario because it only has only 1 time-point, 1721s. This scenario is a so-called steady state scenario, where the plasma current is largely provided by the plasma itself (bootstrap current). This corresponds to the last phase of ITER (> 2038). The composition of the plasma can be seen in Table 6. The properties of the scenario such as confinement regime, magnetic field strength, main species and plasma current can be seen in Table 7. This predictive scenario can be found under shot number 131036, run number 20 in ITER Database.

Species:	D	T	He3	He4	H	Be	Ne
A:	2.0e+00	3.0e+00	3.0e+00	4.0e+00	1.0e+00	8.0e+00	2.0e+01
Z:	1.0e+00	1.0e+00	2.0e+00	2.0e+00	1.0e+00	4.0e+00	1.0e+01
n_over_ntot:	4.5e-01	5.2e-01	5.7e-05	2.9e-03	9.8e-05	2.2e-02	7.8e-03
n_over_ne:	4.0e-01	4.7e-01	5.2e-05	2.6e-03	8.8e-05	2.0e-02	7.0e-03
n_over_n_maj:	8.6e-01	1.0e+00	1.1e-04	5.6e-03	1.9e-04	4.3e-02	1.5e-02

Table 6: Plasma composition deducted from the IDS.

confinement_regime:	VH-Mode
magnetic_field:	-5.30 [T]
main_species:	D-T
plasma_current:	-10.00 [MA]
central_electron_density:	6.11e+19 [m^{-3}]

Table 7: Scenario properties.

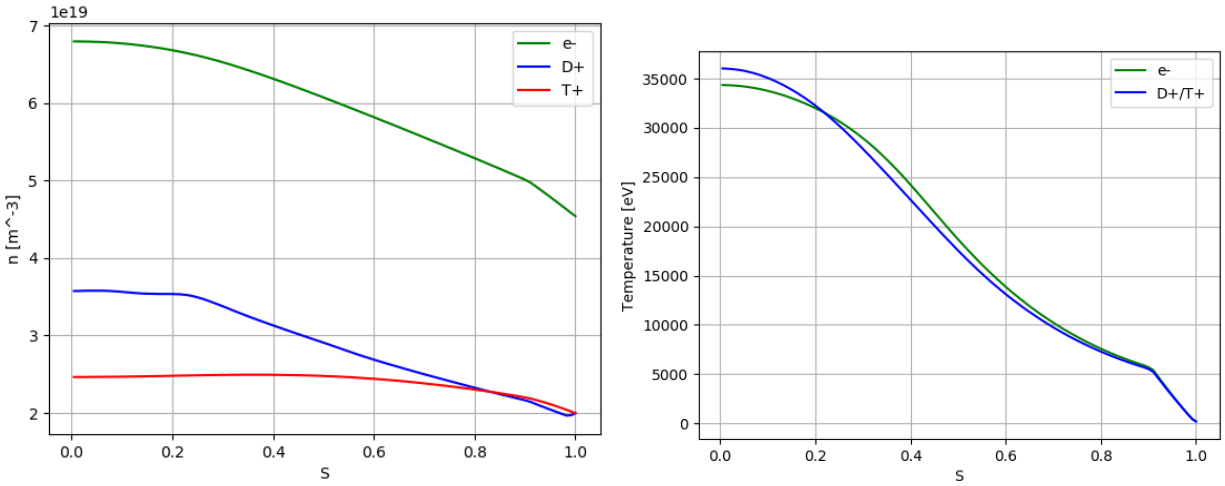

(a) (b)

Figure 24: a) The density profiles of electrons, Deuterium and Tritium, b) The temperature profiles of electrons, Deuterium and Tritium.

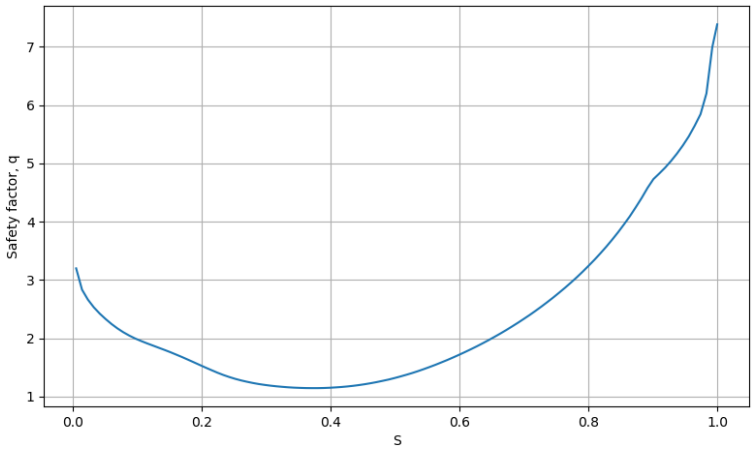

Figure 25: Safety factor, q profile.

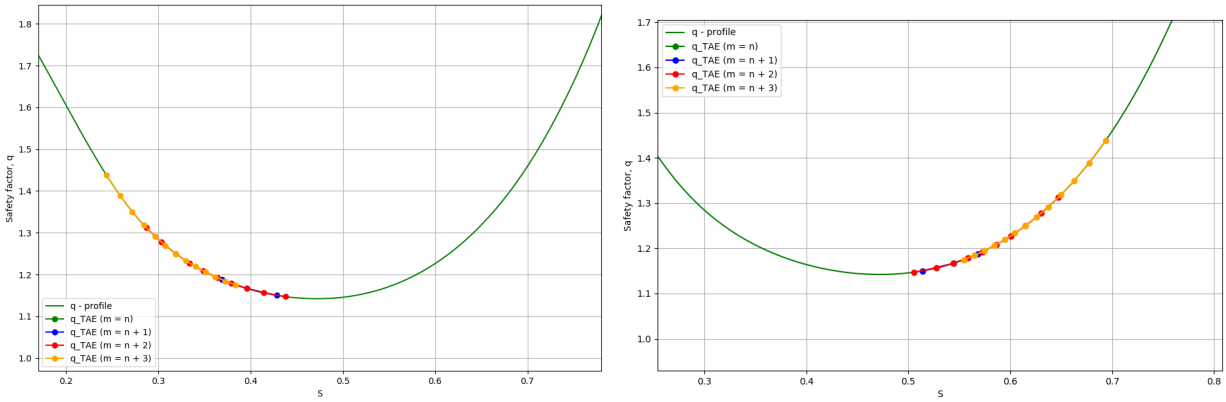

(a) (b)

Figure 26: a) The safety factor (q - profile) and the rational surfaces $q(s_{TAE})$ for $m = n, n+1, n+2, n+3$ with $s_{TAE} < s(q_{min}) \sim 0.5$. b) The safety factor (q - profile) and the rational surfaces $q(s_{TAE})$ for $m = n, n+1, n+2, n+3$ with $s_{TAE} > s(q_{min}) \sim 0.5$.

In figure 25 it can be seen the safety factor, q - profile for this scenario. Because the profile is not monotonic, 2 branches of roots for TAEs are expected. One branch with $r_{TAE} < 0.5$ and another branch with $r_{TAE} > 0.5$ (figure 26). Also, since q has no value around 1, we can expect that the modes with $n = m$ will not be found because the TAE rational surface is not in the plasma. In figure 26 a clear distinction between the 2 branches of TAEs has been made. In (a) the q - profile and the rational surfaces $q(s_{TAE})$ for the lower radial positions of the TAE can be found, and in (b) the higher radial positions. Therefore, we can treat the 2 branches separately as can be seen in the next section.

5.3.1 Low toroidal mode numbers

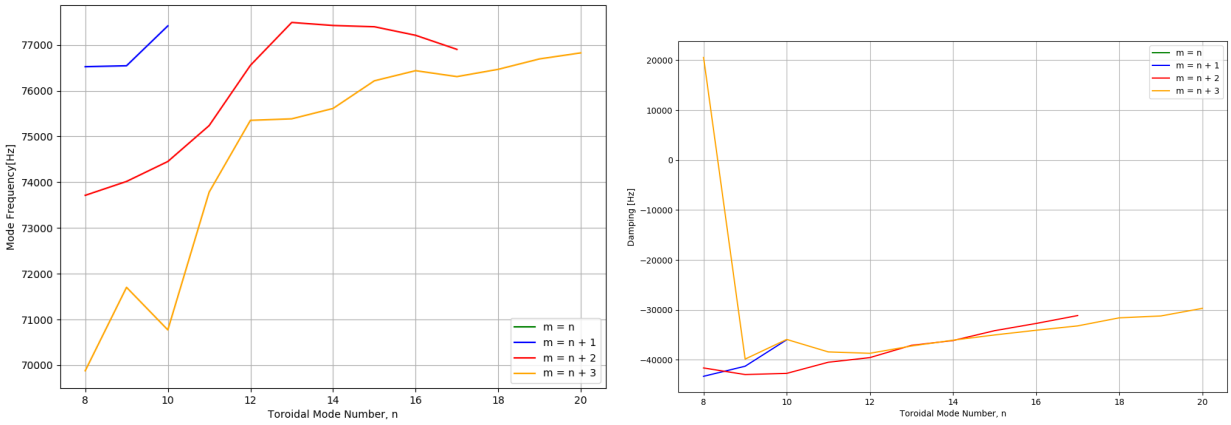

(a) (b)

Figure 27: a) Mode Frequency vs Toroidal Mode Number for 4 different poloidal mode numbers $m = n, n+1, n+2, n+3$ with $s_{TAE} < s(q_{min}) \sim 0.5$. b) Damping vs Toroidal Mode Number for 4 different poloidal mode numbers $n = n, n+1, n+2, n+3$ with $s_{TAE} < s(q_{min}) \sim 0.5$.

Firstly, the branch with $s_{TAE} < s(q_{min}) \sim 0.5$ (inner side) is investigated and in figure 27 plots for mode frequency (a) at different toroidal mode numbers for $m = n, n+1, n+2, n+3$ can be found, and in (b) the damping of those modes. As expected, no modes for $m = n$ were found, and very few modes for $m = n+1, n+2$. Generally, modes with $m = n+3$ are not of interest, because they do not pose a problem in terms of stability. Also, one can observe that the frequency preserves the same shape as seen before, for the same toroidal mode number n, the smallest m has a higher frequency. In (b) the damping of these modes is plotted, we can see that the local solver has an error at $n = 8$ for the $m = n+3$ mode because the damping of the mode becomes positive, this is not correct and it will be investigated in a future release of the workflow.

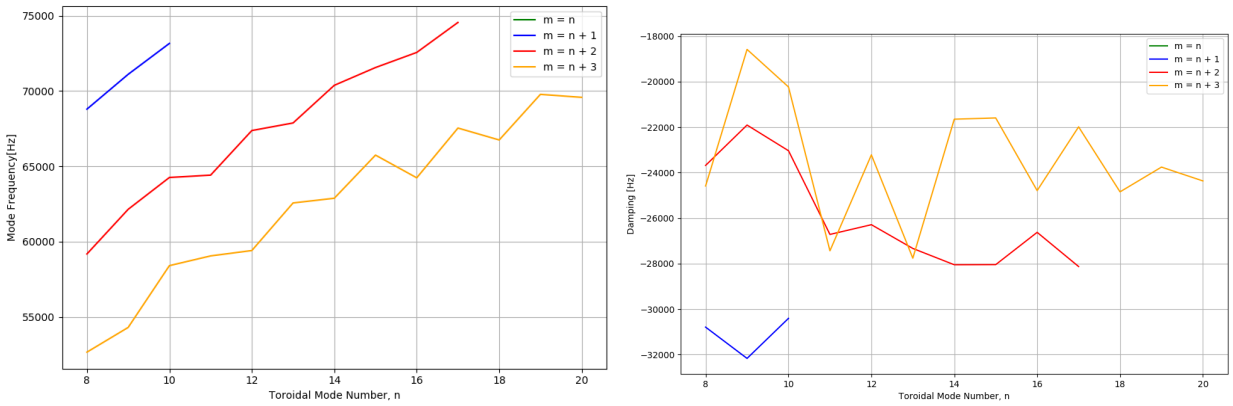

(a) (b)

Figure 28: a) Mode Frequency vs Toroidal Mode Number for 4 different poloidal mode numbers $m = n, n+1, n+2, n+3$ with $s_{TAE} > s(q_{min}) \sim 0.5$. b) Damping vs Toroidal Mode Number for 4 different poloidal mode numbers $n = n, n+1, n+2, n+3$ with $s_{TAE} > s(q_{min}) \sim 0.5$.

The branch with $s_{TAE} > s(q_{min}) \sim 0.5$ (outer side) is plotted if figure 28. As expected, the modes with $m = n$ are not present, again, due to the q - profile minimum value being far away from 1. The modes that are found, decrease in frequency as m gets larger, for each n. In (b) one can see that the modes which are closer to the core (smaller m) are more damped than the ones outside, due to the increased ion density in the core (ion Landau Damping).

Except for a few cases that will need further investigations, the workflow is shown to successfully estimate the local properties of TAEs in time - dependent and time - independent scenarios. Overview type studies give clear indications where and at what time point a global investigation is necessary.

6 Global simulation of energetic particle driven modes in ITER (mode 5, 4 and 1)

6.1 DT Plasma with 5.3T and 15 MA (Time - Dependent)

A second time-dependent scenario generated by METIS, a Deuterium - Tritium plasma is considered. This scenario is supposed to be the standard for $Q = 10$ ITER baseline DT plasma and thus one of the most important scenarios for fusion of ITER. A time evolution of the plasma is considered in 108 timesteps. Out of those, for mode 5, 85 were selected and the same for mode 4 and later mode 1. This is due to the fact that HELENA does not converge in the first 14 time-points as given by the transport code. In Table 8 we can see that in this case we have a higher population of fast particles present in the plasma and thus, they will be considered in the analysis. The plasma properties such as confinement regime, magnetic field strength, fuelling and plasma current can be seen in Table 9. This predictive scenario can be found under shot number 130012, run number 2 in ITER Database.

Species:	H	D	T	He3	He4	Be	O	W
A:	1.0	2.0	3.0	3.0	4.0	9.0	16.0	183.0
Z:	1.0	1.0	1.0	2.0	2.0	4.0	8.0	74.0
n_over_ntot:	1.18e-20	0.468	0.469	0.045	1.83e-03	0.016	1.62e-04	3.82e-05
n_over_ne:	1.07e-20	0.427	0.428	0.041	1.67e-03	0.015	1.48e-04	3.49e-05
n_over_n_maj: 2.51e-20	2.51e-20	0.997	1.000	0.096	3.90e-03	0.035	3.46e-04	8.14e-05

Table 8: Plasma composition deducted from the IDS.

Confinement regime:	H-L-H
Magnetic field:	-5.30 [T]
Main species:	D-T
Plasma current:	-15.00 [MA]
Central electron density:	1.01e+20 [m^{-3}]

Table 9: Scenario properties.

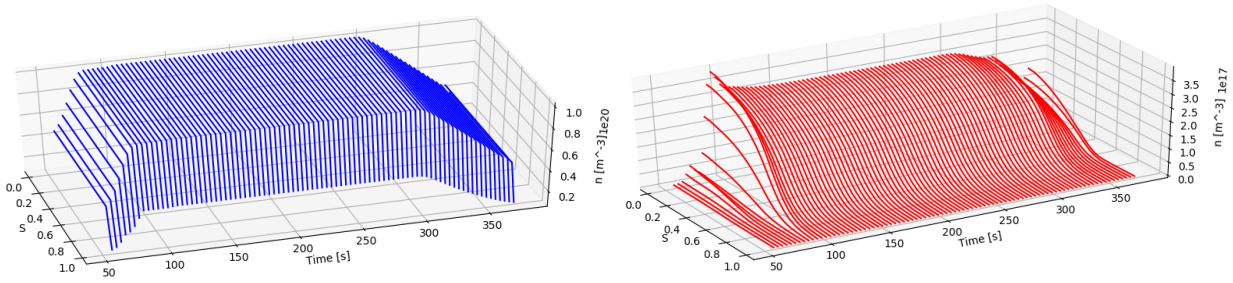

(a) (b)

Figure 29: Time evolution of a) The electron density profile, b) The fast particle density profile.

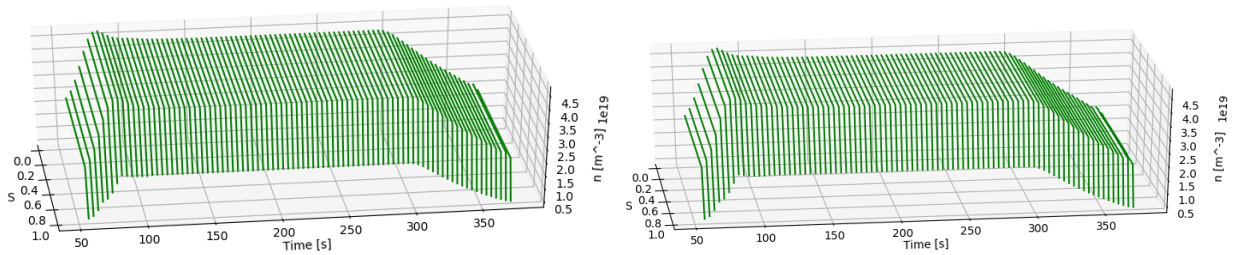

(a) (b)

Figure 30: Time evolution of a) The Deuterium density profile, b) The Tritium density profile.

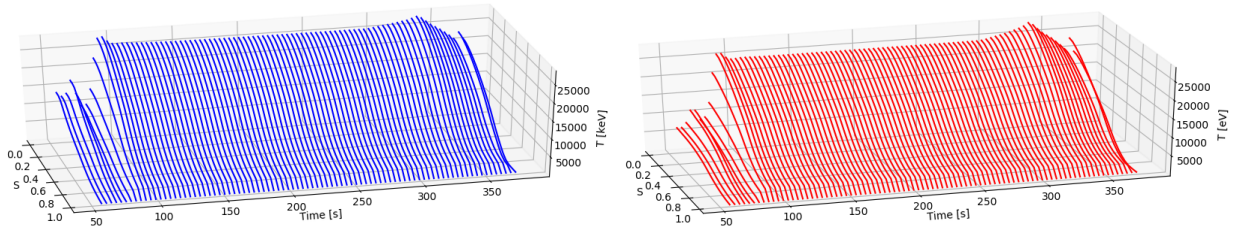

(a) (b)

Figure 31: Time evolution of a) The electron temperature profile, b) The fast particle temperature profile.

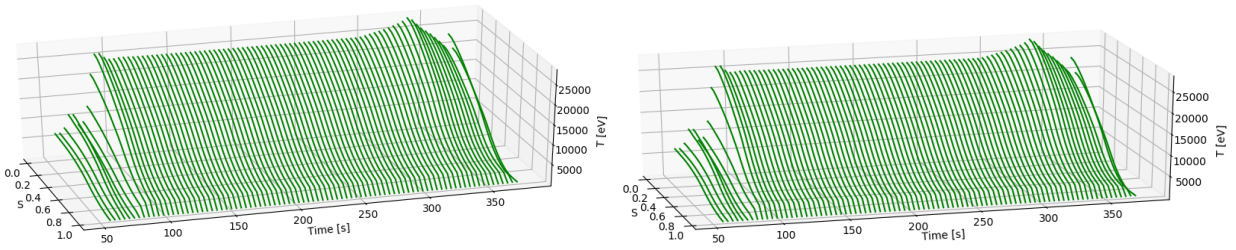

(a) (b)

Figure 32: Time evolution of a) The Deuterium temperature profile, b) The Tritium temperature profile.

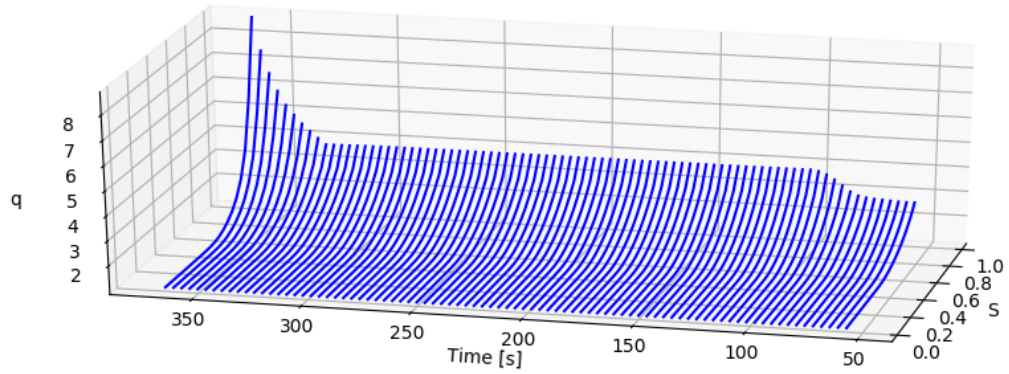

Figure 33: Time dependence of the q profile.

In previous figures the time evolution of the electron, deuterium, tritium and alpha particles density and temperature as well as safety factor profile (q) were plotted as read from the core_profiles_IDS. This give us a general overview of both the properties of the time-dependent scenario and the expected results that follow the stability analysis. For the latter, in order to get an accurate description one needs to look at shorter timescales. For this purpose the scenario was split in ramp-up (60s - 100s) and flat-top (100s - 325s). In the following part, both of the intervals were analyzed with respect to the TAE properties.

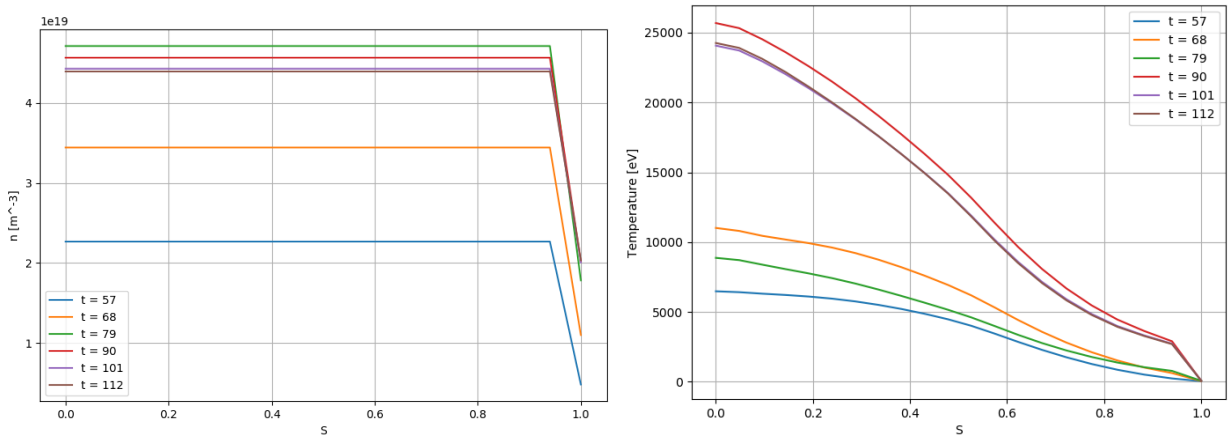

(a) (b)

Figure 34: Time evolution in the ramp-up phase of a) the deuterium density profile, b) the deuterium temperature profile.

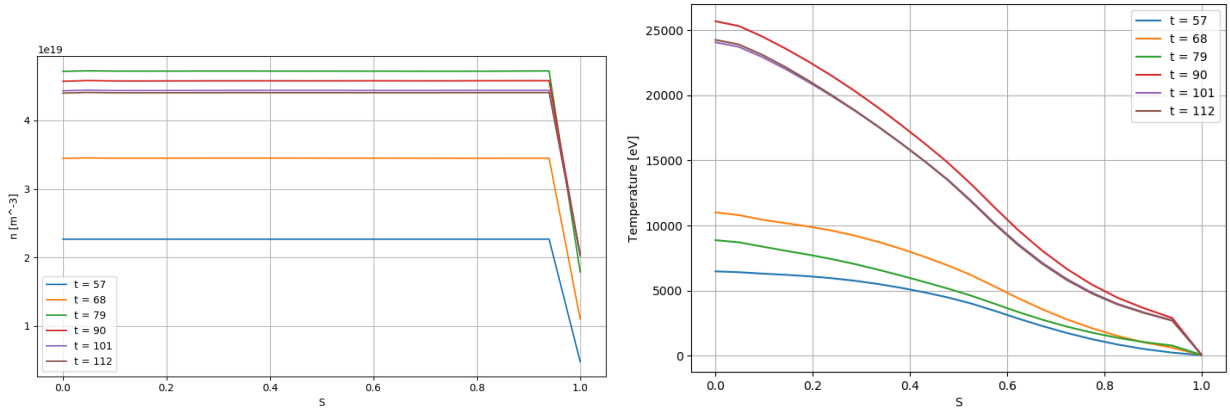

(a) (b)

Figure 35: Time evolution in the ramp-up phase of a) the tritium density profile, b) the tritium temperature profile.

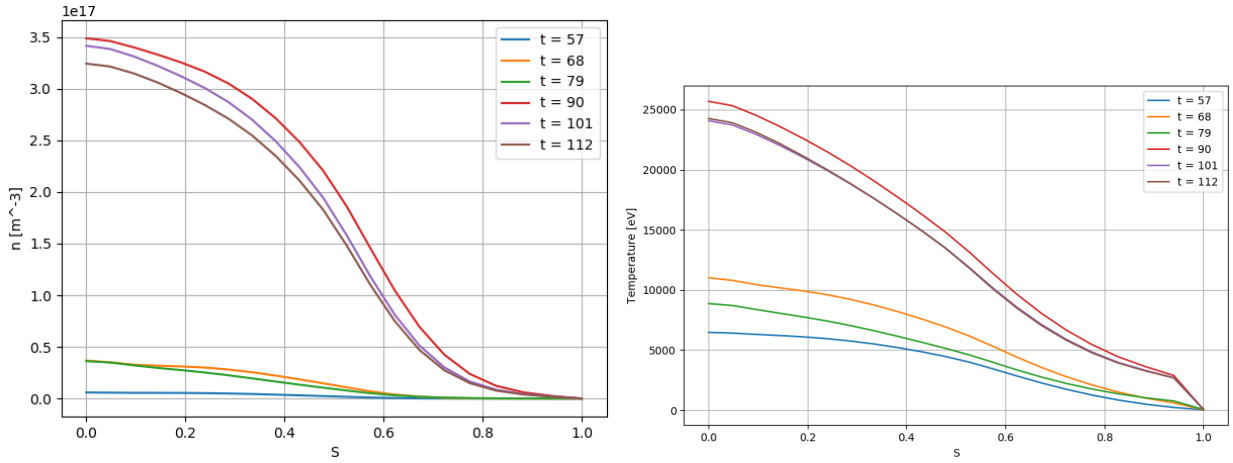

(a) (b)

Figure 36: Time evolution in the ramp-up phase of a) the alpha particles density profile, b) the alpha particles temperature profile.

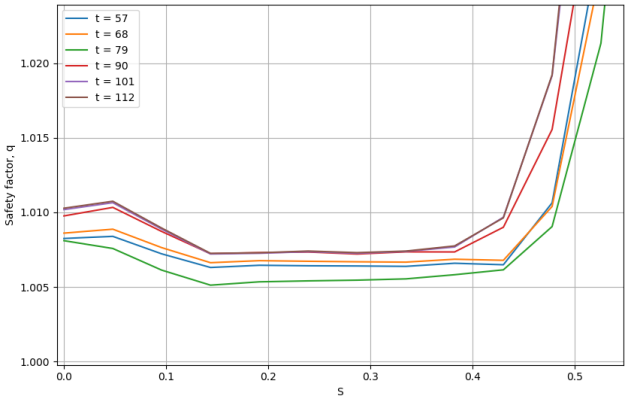

Figure 37: Time dependence of the q profile in the ramp-up phase.

In the ramp-up phase, it can be noticed that the densities of Deuterium, Tritium and α - particles are increasing. As expected, the energetic particles density increase is delayed when compared to the ions density. This is due to the fact that the temperatures of Deuterium and Tritium are not yet sufficiently high to achieve significant fusion and thus, α - particles. By comparing Figure 36(a) (time evolution of alpha particle density profile) with Figure 34(b)/Figure 35(b) (time evolution of Tritium/Deuterium temperature profile) one can easily observe that for $t = 57, 68, 79$ both the ion's temperatures and fast particle density are low, only after $t = 90$ we observe an increase in both, simultaneously.

In Figure 37 the time dependence of the safety factor (q) profile during the ramp-up phase is displayed. It can be seen that the profile changes over time, due to the evolution of the plasma current. Again, it is slightly reversed (see chapter 5.3) at some time-points which means that the profile is not monotonic. The ions density, temperature and the q - profile variation will directly influence the frequency and the damping of the Toroidal Alfvén Eigenmodes (TAE) which will be investigated.

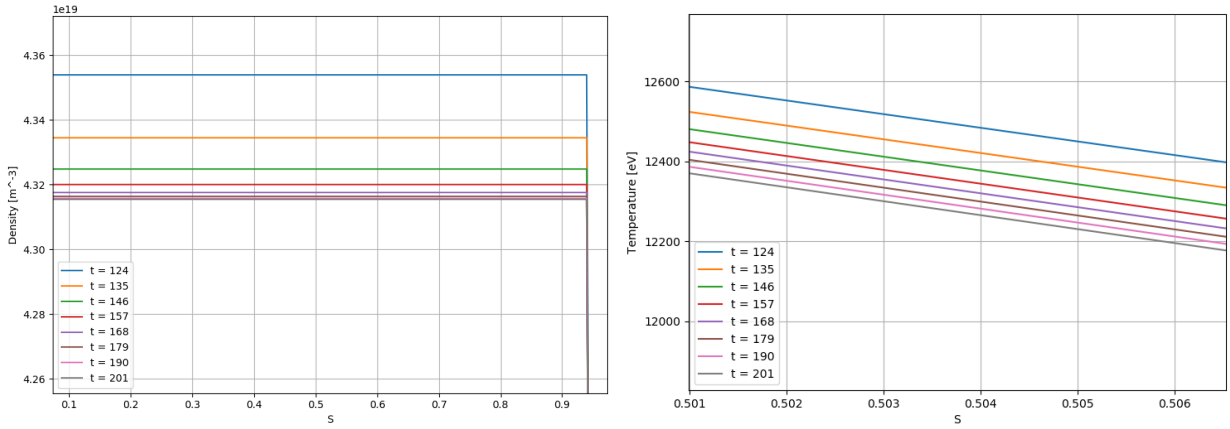

(a) (b)

Figure 38: Time evolution in the flat-top phase of a) The Deuterium density profile, b) The Deuterium temperature profile.

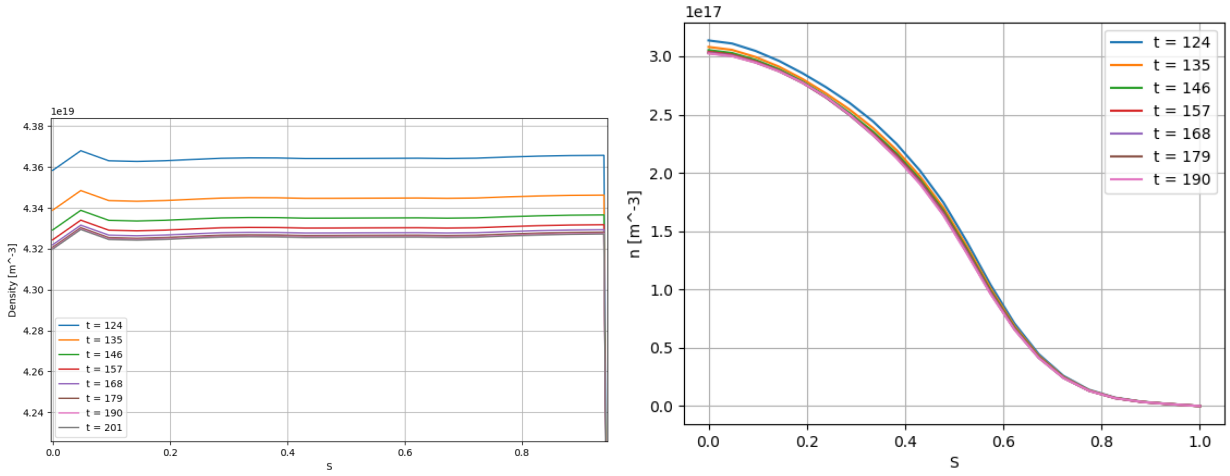

(a) (b)

Figure 39: Time evolution in the flat-top phase of a) The Tritium density profile, b) The alpha particles density profile.

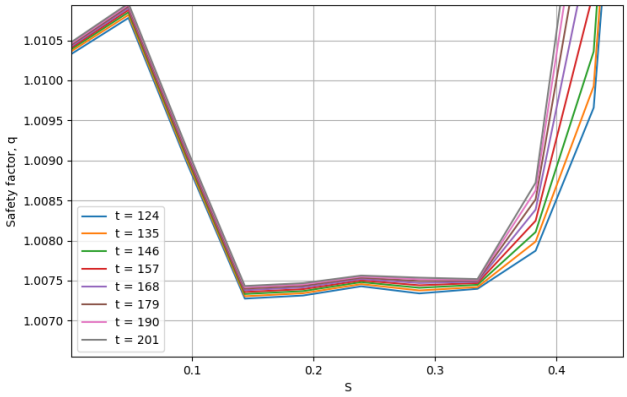

Figure 40: Time dependence of the q profile in the flat-top phase.

While in the ramp-up phase of the plasma evolution time dependant fluctuations of density, temperature and q - profile are expected (and thus finding different instabilities patterns also expected), during the flat-top phase of the scenario, only very small oscillations from one time-point to another should take place. In Figure 38 the density and temperature of Deuterium can be seen at different time-points during the flat-top phase. It can be seen that the density from $t = 124$ to $t = 135$ is of approximately $\Delta n \simeq 0.02 \cdot 10^{19} m^{-3}$ and then again the same to $t = 168$. In the same manner, the Deuterium temperature is decreasing with time $\Delta T \simeq 200$ eV. These variations will lead to variations in the frequency and damping of TAEs. In Figure 39 the density profile of Tritium for different time-points shows that the density not only fluctuates in time , but radially as well (see $s = 0.0 - 0.2$). Because of this, and the q - profile variations (especially being non - monotonous radially) one can expect, multiple number of modes with the same toroidal mode number n and poloidal mode number m to be found having different frequencies and damping rates in different radial locations.

6.1.1 Low toroidal mode numbers

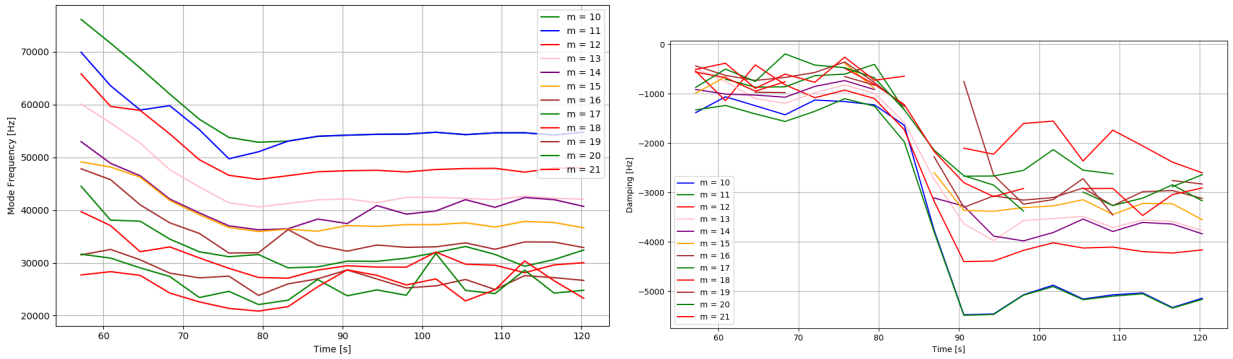

(a) (b)

Figure 41: Time evolution of a) TAE frequency found for $n = 10$ for different m without considering alpha particles. b) TAE damping for $n = 10$ with no alpha particles present - mode 4.

In Figure 41 (a) can be seen the frequency of the modes found with $n = 10$ for different m without considering alpha particles resulting from running LIGKA mode 4 (local calculation). In the ramp-up phase ($t = 60s - 80s$), as expected, these modes have a higher frequency because the ramp-up of density ($v_A \sim \frac{1}{\sqrt{n}}$) and temperature of the ions (Deuterium and Tritium) are bigger. After $t = 80s$, in the flat-top region a smaller but slowly varying mode frequency can be noticed. It can be seen that the frequency decreases with increasing m. This is also expected because an increasing poloidal mode number means that the mode is further away from the core of the plasma. Because the modes far away from the center of the plasma are in general considered harmless since they are not in steep α - gradient region, the focus is on the first three m ($m = 10, 11, 12$). In Figure 41 (b) the time dependence of the damping rate of the modes is displayed. It can be noticed that for $m = 12$ (red line) there were jumps in the damping at $t = 72s$, $t = 94s$ and $t = 109s$ this is due to the fact that multiple modes were found for the same toroidal and poloidal mode number at different radial locations. As explained before, these modes have been taken out from the damping analysis because they are not of interest. This is due to the non-monotonous behaviour of the q - profile (as explained above). These jumps will be

automatically removed in the next version of the workflow since they are nonphysical and not relevant (the most important ones $m < n + 5$).

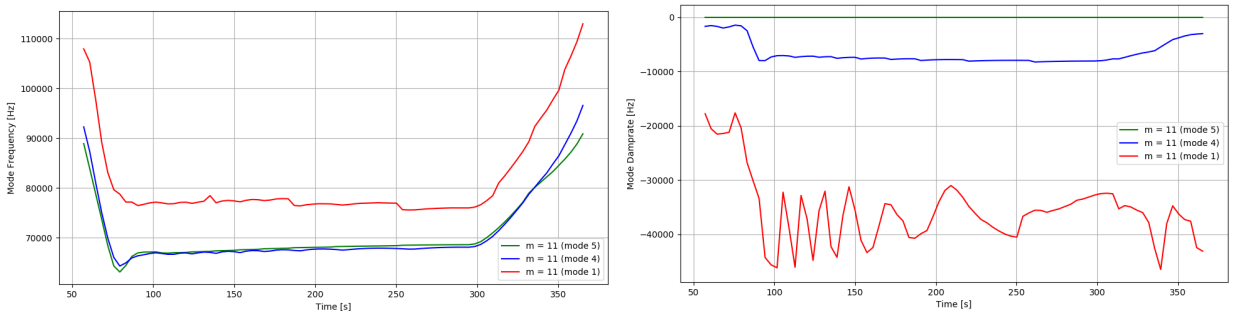

(a) (b)

Figure 42: Time evolution of a) TAE frequency found for $n = 10$ and $m = 11$ without alpha particles present. b) TAE damping rate for $n = 10$ and $m = 11$ without alpha particles present - comparison with mode 1 (global).

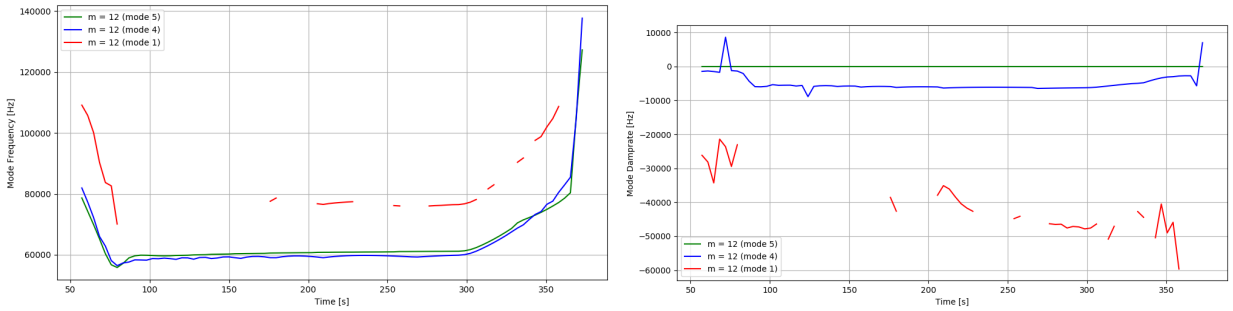

(a) (b)

Figure 43: Time evolution of a) TAE frequency found for $n = 10$ and $m = 12$ without alpha particles present. b) TAE damping rate for $n = 10$ and $m = 12$ without alpha particles present - comparison with mode 1 (global).

As discussed before, the modes that present interest for the stability analysis are the ones close to the core of the plasma. In Figures 42 and 43 the TAE frequency (a) and damping rate of modes with $n = 10$ and $m = 11, 12$ are displayed. This is done by doing a comparison between mode 5,4 (local solver) and mode 1 (global solver). It can be clearly seen that the mode 5 and mode 4 give similar results in both cases for the frequency (mode 4 more accurate than mode 5). Mode 1, being a global solver is much more expensive to run, but at the same time, the results are more accurate. Typically the difference between a

global calculation and a local one is of 10%, which is in agreement with the one displayed in both frequency graphs. The bigger difference between mode 4 results and mode 1 can bee seen in damping, again, with mode 1 being much more accurate. For $m = 11$ the damping in the ramp-up phase behave the same in both mode 4 and mode 1 (respecting the proportions). The difference can be seen in $t > 100$ where the flat-top of the plasma profile is. The fluctuations in damping present here are due to the fluctuations presented before in the ion density and the q - profile. A change in the density or safety factor can lead to an exponential change in the damping of the modes. For $m = 12$ it can be noticed that not for all time-points the global solver found modes. This is due to the threshold of the global solver in damping which is set at 10%. Which means, all modes that are damped over this value, will not be considered to have an impact on the stability of the plasma and are ignored. This demonstrates the the local solvers give a good overview of the modes, while the global one gives a more in depth analysis.

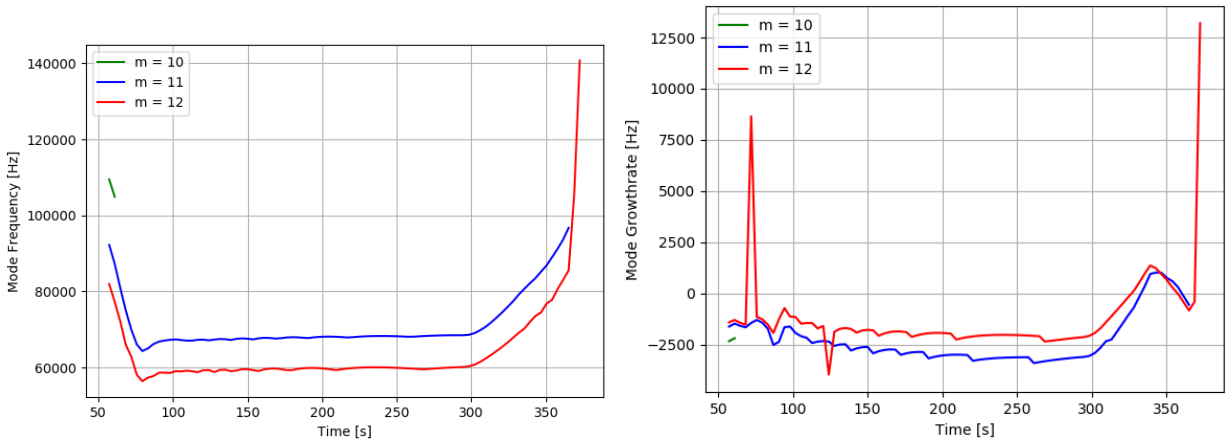

(a) (b)

Figure 44: Time evolution of a) TAE frequency found for $n = 10$ for the first three m with alpha particles present. b) TAE growth/damping for $n = 10$ with alpha particles present - mode 4.

In the figure 44 above, the time evolution of the TAE frequency and damping with alpha particles is displayed for $n = 10$ and $m = 10, 11, 12$ as given by the local solver (mode 4). Same as in the case without alpha particles, $m = 10$ is not found only in the

first 2 time-points of the run and the most significant ones that remain important over the course of the whole simulation are $m = 11, 12$. The difference from the previous case is given by the alpha particle density variation (see Figure 39(b)). As before, the presence of a non-monotonous radially and varying in time q - profile gives the spikes in damping that can be seen in (b) at time-points $t = 60s, 120s, 360s$. This is due to finding mode than one mode with the same toroidal mode number and poloidal mode number at different radial locations. The influence of alpha particles on the stability is seen as they drive the modes unstable around time-point $t = 340s$.

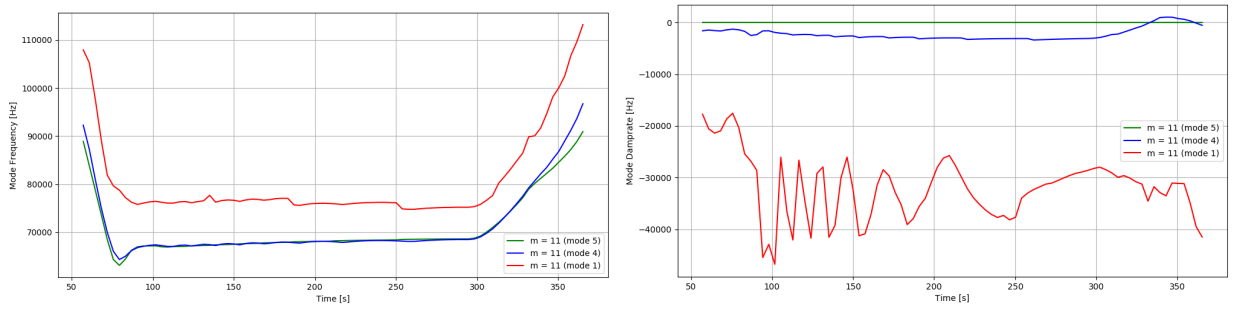

(a) (b)

Figure 45: Time evolution of a) TAE frequency found for $n = 10$ and $m = 11$ with alpha particles present. b) TAE damping rate for $n = 10$ and $m = 11$ with alpha particles present - comparison with mode 1 (global).

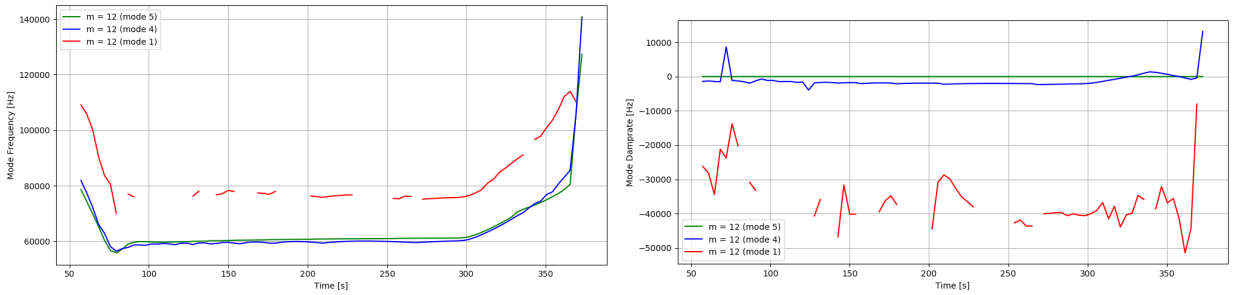

(a) (b)

Figure 46: Time evolution of a) TAE frequency found for $n = 10$ and $m = 12$ with alpha particles present. b) TAE damping rate for $n = 10$ and $m = 12$ with alpha particles present - comparison with mode 1 (global).

By taking separately $m = 11$ and $m = 12$ a comparison of the local solver with the global one can be made in the presence of alpha particles. In Figure 45 (a) can be seen that

the frequency of the modes do not change that much in the presence of alpha particles, but because of the alpha particle density variation, especially at $t > 200s$, we can observe small fluctuations in frequency when compared to the same case without alpha particles present (described above). With regards to the damping rate of the modes, the change is more visible, especially after the alpha particle density has increased enough that a significant population is present. A big difference can be noticed in the global solver (mode 1) at $t > 250s$ when the modes are being less damped due to the alpha particle drive. For $m = 12$ (Figure 46) the same behaviour can be observed with some time-points having the modes very damped (over the 10% threshold established in the global solver) and such they do not have an effect on the stability of the plasma. Much like $m = 11$, a decrease in the damping can be noticed after 250s due to the alpha particles. It is important to say that mode 1 damping is much larger than mode 4 damping (explained bellow).

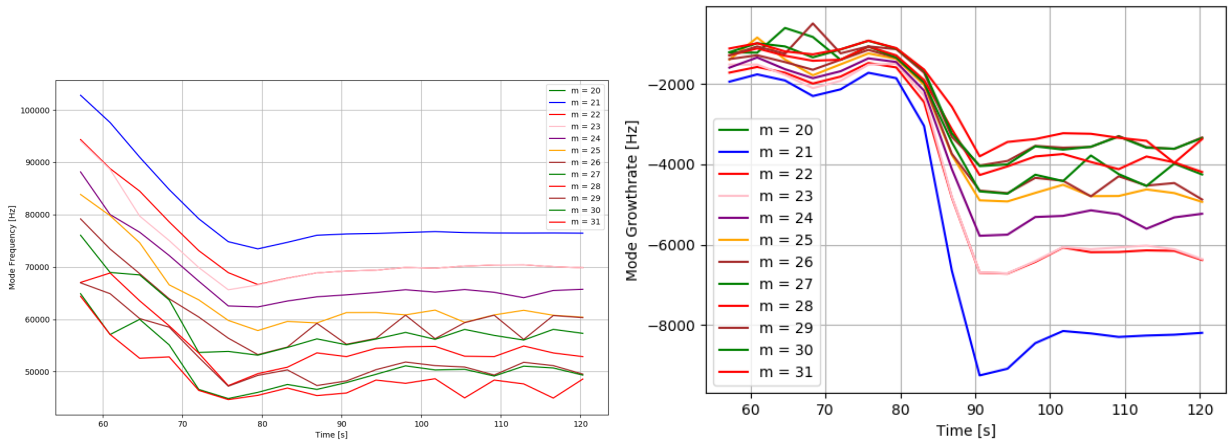

(a) (b)

Figure 47: Time evolution of a) TAE frequency found for $n = 20$ for different m without considering alpha particles. b) TAE growth/damping for $n = 20$ with no alpha particles present - mode 4.

In Figure 47 the time evolution of the TAE frequency and damping for $n = 20$ and different m are displayed without taking into account the alpha particles as given by mode 4. The same trend as before can be observed in terms of mode frequency with $m = 20$ not

being found at all over the 120s of the run. As we move towards the flat-top of the run ($t > 80s$) a decrease in mode frequency can be found, also the modes with higher m have a lower frequency, but at the same time are less damped (compared to $m = 21$).

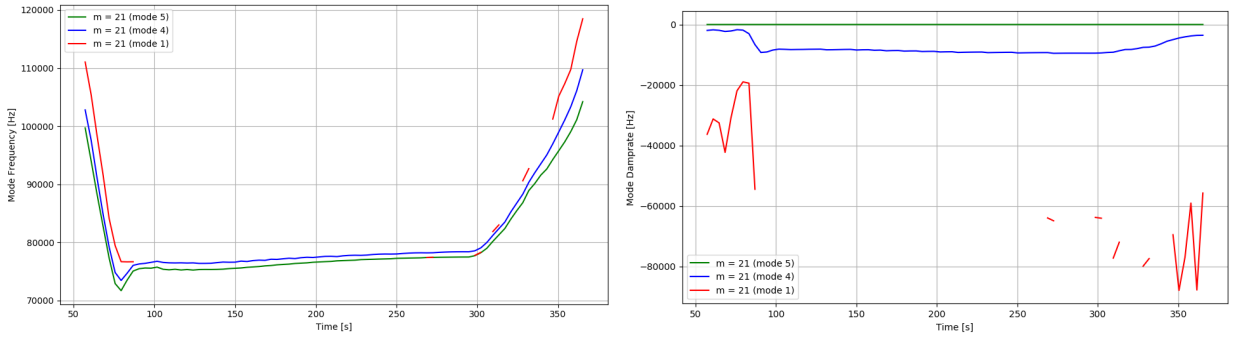

(a) (b)

Figure 48: Time evolution of a) TAE frequency found for $n = 20$ and $m = 21$ without alpha particles present. b) TAE damping rate for $n = 20$ and $m = 21$ without alpha particles present - comparison with mode 1 (global).

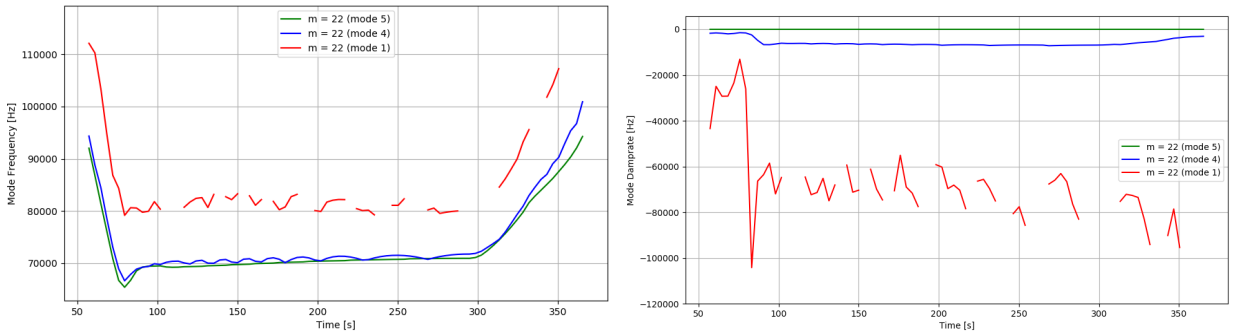

(a) (b)

Figure 49: Time evolution of a) TAE frequency found for $n = 20$ and $m = 22$ without alpha particles present. b) TAE damping rate for $n = 20$ and $m = 22$ without alpha particles present - comparison with mode 1 (global).

Taking the same way two most relevant poloidal mode numbers ($m = 21, 22$) a comparison between mode 4 and mode 1 was plotted in the figures above. For $m = 21$ in the ramp-up and ramp-down the global solver is agreeing more with the local solver. As before, where the global solver found damping rates bigger than 10%, the modes were not considered significant. For $m = 22$, presented in Figure 49, the frequency calculated

by the local solver agrees within 10% margin to the global solver results. In both mode 4 and mode 1 oscillations in the flat-top can be noticed. These are due to the ion density fluctuations over different time-steps. While the frequency of the modes has a linear dependency on the ion density, the damping oscillates on a bigger level due to the great sensitivity to the background profile shape.

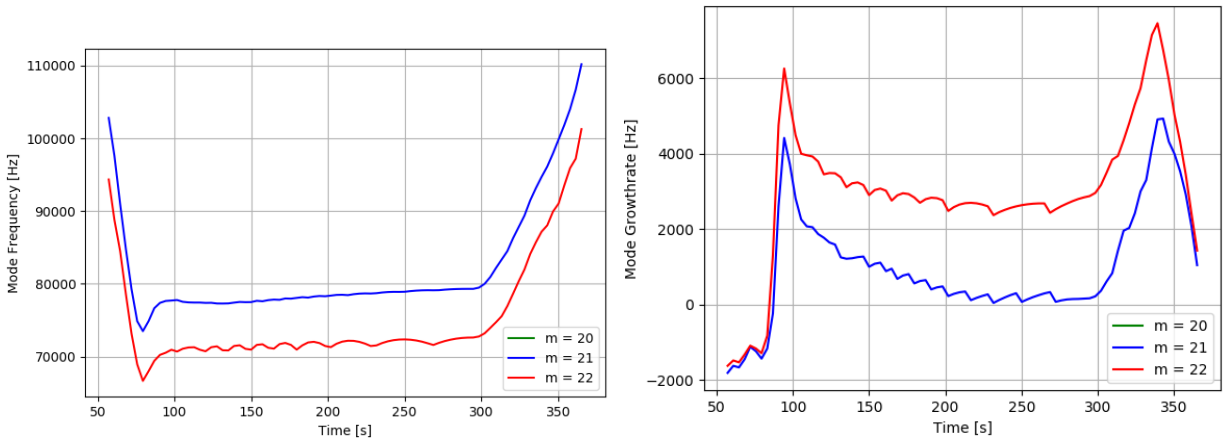

(a) (b)

Figure 50: Time evolution of a) TAE frequency found for $n = 20$ for the first three m with alpha particles present. b) TAE growth/damping for $n = 20$ with alpha particles present - mode 4.

When alpha particles are present for $n = 20$ time evolution of $m = 20, 21, 22$ can be seen in Figure 50. The local solver (mode 4) found modes for $m = 21, 22$. In (a) the frequency of the modes during the run can be seen, with decreasing/increasing frequency during the ramp-up and ramp-down. A good example of alpha-particle drive can be seen in (b) where the alpha-particle drive the modes growthrate from $t = 80s$ where the alpha particle density is sufficiently large until $t = 340s$ in the ramp-down. The oscillations in both the frequency and the growthrate during the flat-top region ($t = 100s - 300s$) are due to the oscillations of the α - particle density in time (as explained in the beginning of the chapter).

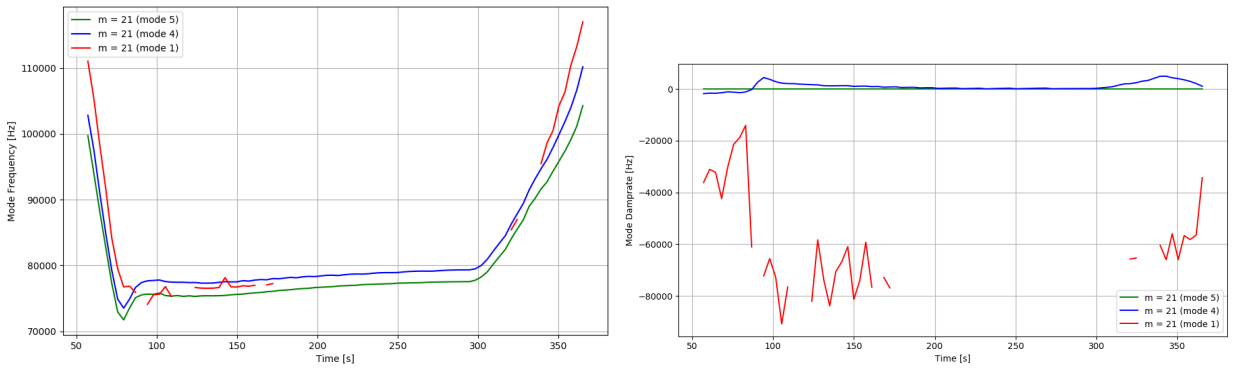

(a) (b)

Figure 51: Time evolution of a) TAE frequency found for $n = 20$ and $m = 21$ with alpha particles present. b) TAE damping rate for $n = 20$ and $m = 21$ with alpha particles present - comparison with mode 1 (global).

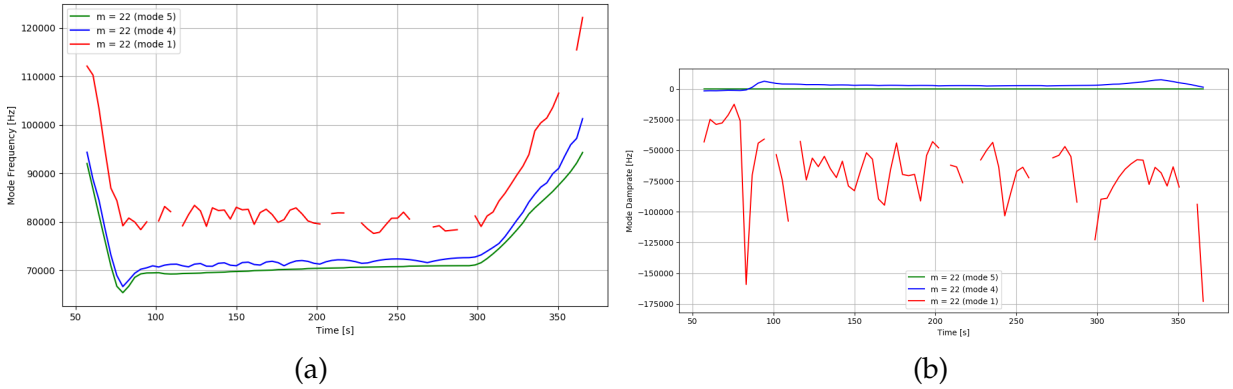

(a) (b)

Figure 52: Time evolution of a) TAE frequency found for $n = 20$ and $m = 22$ with alpha particles present. b) TAE damping rate for $n = 20$ and $m = 22$ with alpha particles present - comparison with mode 1 (global).

In the figures 52 above the time evolution of TAE frequency and damprate in the presence of alpha particles can be observed for $m = 21, 22$ by comparing the results from the local and global solver. For $m = 21$ the global solver frequency result agrees with the mode 4 result and more, it removes the modes that have no significant impact on the stability (Figure 51 $t = 170s - 320s$). For $m = 22$ mode 1 find more stable modes. The variation seen in the frequency is due to the alpha particle density and Deuterium/Tritium density change over time. Here it can be noticed that the frequency oscillations between mode 4 and mode 1 are almost in phase which confirms the findings.

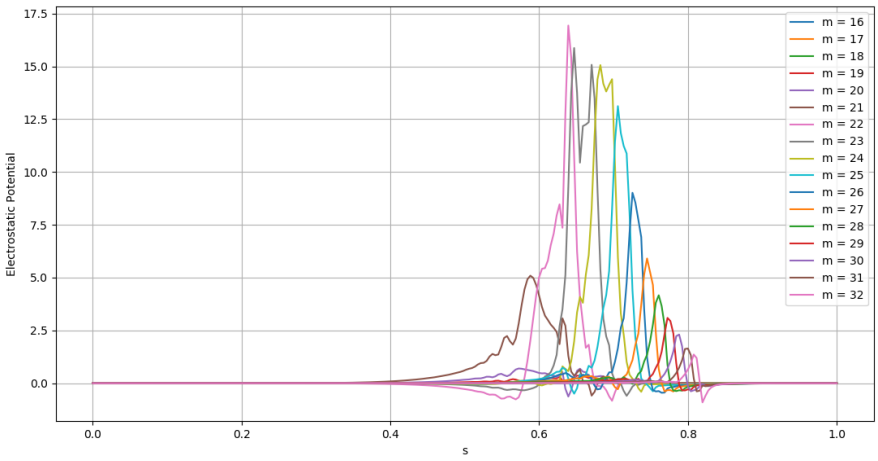

Figure 53: Mode structure for $n = 20$, $m = 22$ for $t = 128s$ with alpha particles.

For a better understanding of the behaviour of TAEs, especially the damping of the modes (difference between mode 4and mode 1), once can have a look at the mode structure seen in figure 53. The resonant TAE locations are very close to each other, which means that the radial harmonics seen above are very strongly peaked. The have a very small scale structure due to the q - profile (derivative of the q - profile, shear). The radiative damping in these modes is very strong, and a reason why one can observe a big difference between mode 4 (local solver) and mode 1 (global solver) is that the local one does not take into account this damping. Around $s \sim 0.8$ one can observe the continuum damping which is always present by the small negative spike in the TAE structure (last gaussian, here pink). For the local solver, this is not included also, because it does not know where the continuum is being reached. E.g. For the poloidal harmonic $m = 21$, denoted by the brown curve in the figure above, one can observe the manifestation of radiative damping: a short radial kinetic Alfvén wave is superimposed on the global TAE structure.

6.1.2 High toroidal mode numbers

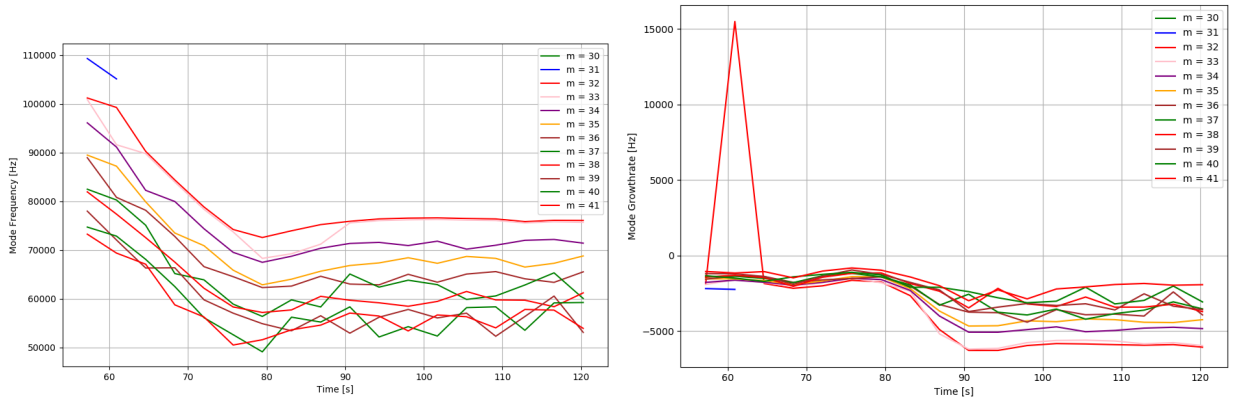

(a) (b)

Figure 54: Time evolution of a) TAE frequency found for $n = 30$ for different m without considering alpha particles. b) TAE growth/damping for $n = 30$ with no alpha particles present - mode 4.

For high toroidal mode numbers,in figure 54 the time dependence of frequency and damprate given by mode 4 (local solver) is presented for $n = 30$. Here one can see that for $m = 30, 31$ the solver cannot find almost any modes, as such the only m that will be investigated is $m = 32$. For this poloidal mode number, in the damping a jump was noticed, this was due to the q - profile variation and finding two modes at different locations with the same n and m, this has been removed from the plot for the reason explained in previous chapters.. After that the modes behave as expected, the damping rate grows as it approaches the flat-top region.

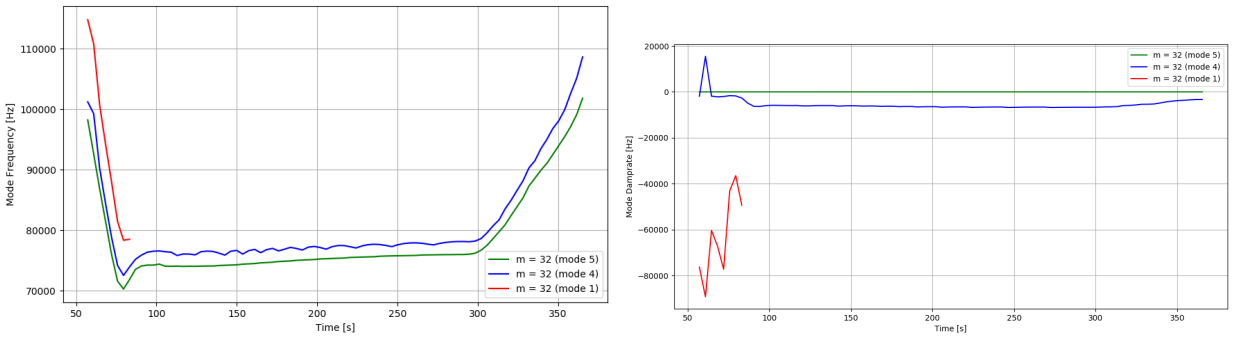

(a) (b)

Figure 55: Time evolution of a) TAE frequency found for $n = 30$ without alpha particles present. b) TAE damping rate for $n = 30$ without alpha particles present - comparison with mode 1 (global).

A closer look at the difference between mode 1 and mode 4 frequency and damping can be found in Figure 55. As the local solver finds damped modes across the run for $m = 32$, the global solver only finds modes in the ramp-up phase because the rest are too strongly damped (over 10%). This is an example of how the local solver, in its present form can be used to have an overview of the potentially dangerous modes, but in the end, a global solver is needed in order to find a more accurate description of the stability.

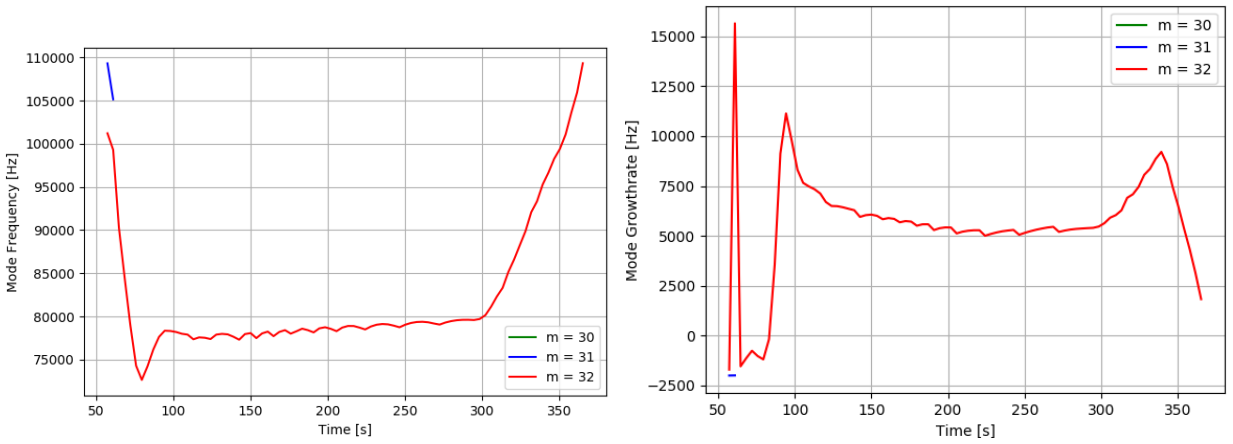

(a) (b)

Figure 56: Time evolution of a) TAE frequency found for $n = 30$ for the first three m with alpha particles present. b) TAE growth/damping for $n = 30$ with alpha particles present - mode 4.

If alpha particles are included in the run, again, the drive is not strong enough for mode 4 to detect any other modes for $n = 30$ and $m = 30, 31$ as can be seen in Figure 56. Only for $m = 32$ modes were found across the run. The $m = 32$ branch becomes unstable just as in $n = 20$ case. This time a significant variation can be found in the growthrate for $t = 60s$, this can be explained by the radial and temporal variation of the q - profile in the ramp-up.

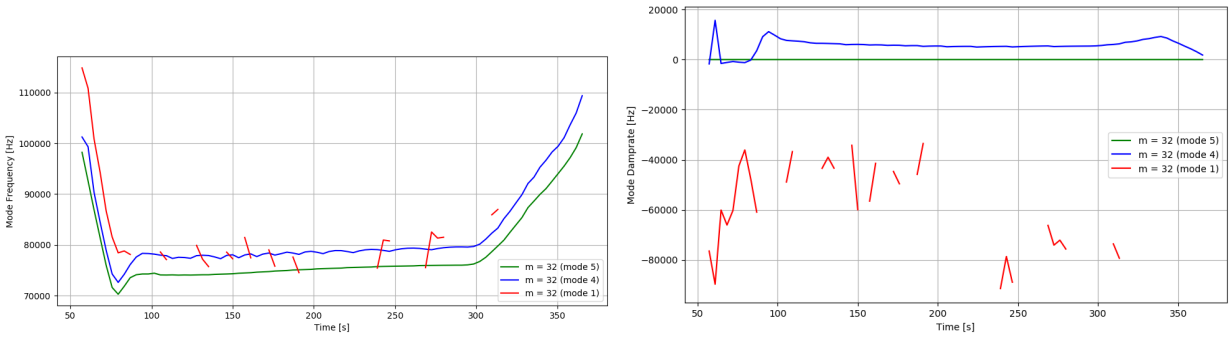

(a) (b)

Figure 57: Time evolution of a) TAE frequency found for $n = 30$ with alpha particles present. b) TAE damping rate for $n = 30$ with alpha particles present - comparison with mode 1 (global).

In Figure 57 a comparison between local and global solver for $n = 30$ and $m = 32$ found modes in the presence of alpha-particle drive is presented. Here, the global solver finds again, less unstable modes than the local solver. For the frequency, one can see that in the ramp-up phase the modes that are found are very close to mode 4 results ($< 10\%$ difference). The same is not true with the flat-top phase, where the global mode is more sensitive to density variations, and such for the modes that it did find a oscillating trend can be seen around the 10% damping rate threshold.

The analysis shows, that for the investigated n, m range no global TAEs are expected to be unstable. This is good news, since the α - confinement is thus not expected to be degraded by TAEs. However, the METIS - given profiles are not necessarily fully realistic. A less flat q - profile can lead to TAE instability.[22]

7 Discussion and Summary

During this thesis, the first energetic particle stability time-dependent workflow which makes use of the new IMAS (Integrated Modelling Analysis Suite) platform was developed with the purpose of meeting the needs of the ITER project. This workflow was tested on 4 ITER predictive scenarios (2 time-dependent and 2 time-independent) by studying the impact of TAE modes. The codes that make up the automated workflow as described in chapter 4 are: HELENA, an equilibrium solver that outputs the MHD equilibrium, the Cubic Hermite Element Axisymmetric Static Equilibrium (CHEASE), a more flexible alternative to HELENA (due to the ability to generate new pressure profiles) and the Linear Gyrokinetic Shear Alfven Physics (LIGKA) code which solves the linearized gyrokinetic equations to find eigenvalues and eigenfunctions of the system (frequency, damping and mode structure as can be seen in chapter 5 and 6). The workflow was implemented in Python by using the IMAS Python Access Layer (IMASPy). To arrive at this stage of the work took almost 1 year and several implementations were necessary in order to decide how the final workflow will look like.

The mode frequency and damping/growth were calculated for 4 scenarios using the workflow: two of them time-dependent, two time-independent. In chapter 5.1 pre-fusion plasma scenario was analyzed in order to get an overview of how the workflow behaves in a time-dependent scenario. To look at the frequency and the damping, for $n = 10, 20, 30$ 12 poloidal mode numbers were analyzed for each n and time-evolution plots of frequency and damping were done. Here, both quantities confirm the dependency of the stability of the modes on density profiles and safety factor profile. The second scenario can be found in chapter 5.2. An analysis was made based on the non - monotonous (slightly reversed) q - profile and 2 branches with modes were found. This run was performed in order to check the multi-species part of the workflow, namely, the deuterium - tritium mix. In the frequency and damping analysis the two separate branches of TAE

were observed and their influence was explained. In chapter 5.3 an advanced scenario was analyzed, which corresponds to the last phase of ITER (>2038). Here, a reversed q - profile was found, and thus the separation of the two TAE branches is very visible. The analysis of the frequency and damping was split in two, one for each branch. The splitting depends strongly on the q_{min} value, which in this case was located at $s \sim 0.5$. In order to find the two separate branches, the rational surfaces of TAE modes for 4 different poloidal mode numbers were plotted in comparison to the q - profile. In the last scenario, chapter 6, the time evolution of the stability of a deuterium - tritium plasma was performed with and without alpha particles for $n = 10, 20, 30$. In this part, also the global solver (mode 1) was used in order to perform a proper comparison with the local solver (mode 4). The results of frequency and damping indicate that mode 1 is more stable due to continuum damping and radiative damping, which are neglected by the local solver. It was seen also that the α - particle gradient was not enough to drive TAEs unstable. According to mode 4 calculations this was the exact opposite. This proves that while the local model gives a overview of the problem and the main points where one should focus computational resources, mode 1 is more reliable and thus should be used in order to get a deeper understanding of the stability. As mentioned above, in this scenario the transport code was generated by METIS, which has several known problems, especially for the realism of the q - profile. On the other hand, the calculations show a path how to design TAE - stable scenarios by tailoring the q - profile, i.e. the plasma current profile.

7.1 Outlook

The next step in further developing the workflow will be consolidation and removal of the remaining problems, together with the improvement of exception handling. Mode 4 needs to be improved to also take into account the radiative damping. Mode 5 (local) improvement for guessing the mode structure in order to have a better estimates about the locality of the modes, which in the future will decide when to run mode 1 (global

mode). The Neutral beam injection (NBI) distribution function will be added, then the non - linear hybrid model (HAGIS 2) will be next, in order to predict the saturation level of modes. Once LIGKA/HAGIS is successfully implemented, the information gathered from the runs will be used to build transport models. And finally, the coupling of the energetic particle transport as given by LIGKA/HAGIS back to transport codes to allow self - consistent treatment.

8 Acknowledgements

I would like to thank Dr. Philipp Lauber as well as the other members of his research group, in particular Dr. Thomas W. Hayward , for their guidance and patience with me. I would also want to thank them for the codes and continuous support they provided to perform the stability analysis. My thanks also go to Dr. Schneider Mireille and Dr. Pinches Simon for providing support for IMAS integration and adaptation of the codes and the workflow. And last but not least my family who has been there for me from the beginning of my studies.

References

(1) Tomabechi, K.; Gilleland, J.; Sokolov, Y.; and, R. T. ITER conceptual design. *Nuclear Fusion* **1991**, *31*, 1135–1224.

(2) Hazeltine, R.; Meiss, J. *Plasma Confinement*; Dover books on physics; Dover Publications, 2003.

(3) Lawson, J. D. Some Criteria for a Power Producing Thermonuclear Reactor. *Proceedings of the Physical Society. Section B* **1957**, *70*, 6–10.

(4) Chen, F. F. *Introduction to Plasma Physics and Controlled Fusion*; Springer International Publishing Switzerland 2016; Springer International Publishing, 2016.

(5) Chen, L.; Zonca, F. Physics of Alfvén waves and energetic particles in burning plasmas. *Rev. Mod. Phys.* **2016**, *88*, 015008.

(6) Pinches, S. Nonlinear interaction of fast particles with Alfvén waves in tokamaks. **2020**,

(7) Mıkhaılovskii, A. B. Thermonuclear "drift" instabilities. *Journal of Experimental and Theoretical Physics* **1975**, *41*, 890–894.

(8) Cheng, C. Z.; Chance, M. S. Low-n shear Alfvén spectra in axisymmetric toroidal plasmas. *The Physics of Fluids* **1986**, *29*, 3695–3701.

(9) Lauber, P.; Günter, S.; Könies, A.; Pinches, S. LIGKA: A linear gyrokinetic code for the description of background kinetic and fast particle effects on the MHD stability in tokamaks. *Journal of Computational Physics* **2007**, *226*, 447–465.

(10) Imbeaux, F.; Pinches, S.; Lister, J.; Buravand, Y.; Casper, T.; Duval, B.; Guillerminet, B.; Hosokawa, M.; Houlberg, W.; Huynh, P. et al. Design and first applications of the ITER integrated modelling & analysis suite. *Nuclear Fusion* **2015**, *55*, 123006.

(11) Landau, L. On the vibration of the electron plasma. *J. Phys. (USSR)* **1946**, *10*, 25–34.

(12) Doveil, F.; Escande, D. F.; Macor, A. Experimental Observation of Nonlinear Synchronization due to a Single Wave. *Phys. Rev. Lett.* **2005**, *94*, 085003.

(13) Hayward-Schneider, T. Global nonlinear fully gyrokinetic and hybrid treatments of Alfvénic instabilities in ITER. Dissertation, Technische Universität München, München, 2020.

(14) Vlasov, A. A. On Vibration Properties of Electron Gas. *Journal of Experimental and Theoretical Physics* **1938**, *3*.

(15) Mishchenko, A.; Bottino, A.; Hatzky, R.; Sonnendrücker, E.; Kleiber, R.; Könies, A. Mitigation of the cancellation problem in the gyrokinetic particle-in-cell simulations of global electromagnetic modes. *Physics of Plasmas* **2017**, *24*, 081206.

(16) Bierwage, A.; Lauber, P. Gyrokinetic analysis of low-n shear Alfvén and ion sound wave spectra in a high-beta tokamak plasma. *Nuclear Fusion* **2017**, *57*, 116063.

(17) Zonca, F.; Chen, L. Theory of toroidal Alfvén modes excited by energetic particles in tokamaks. *Physics of Plasmas* **1996**, *3*, 323–343.

(18) Fesenyuk, O. P.; Kolesnichenko, Y. I.; Yakovenko, Y. V. Geodesic acoustic mode frequency and the structure of Alfvén continuum in toroidal plasmas with highq2. *Plasma Physics and Controlled Fusion* **2012**, *54*, 085014.

(19) Mett, R. R.; Mahajan, S. M. Kinetic theory of toroidicity-induced Alfvén eigenmodes. *Physics of Fluids B: Plasma Physics* **1992**, *4*, 2885–2893.

(20) Huysmans, G.; Goedbloed, J.; Kerner, W. Proceedings of the CP90 Conference on Computational Physics. 1991.

(21) Lütjens, H.; Bondeson, A.; Sauter, O. The CHEASE code for toroidal MHD equilibria. *Computer Physics Communications* **1996**, *97*, 219 – 260.

(22) Pinches, S. D.; Chapman, I. T.; Lauber, P. W.; Oliver, H. J. C.; Sharapov, S. E.; Shinohara, K.; Tani, K. Energetic ions in ITER plasmas. *Physics of Plasmas (1994-present)* **2015**, *22*, –.

(23) Ph, L. Super-thermal particles in hot plasmas—Kinetic models, numerical solution strategies, and comparison to tokamak experiments. *Physics Reports* **2013**, *533*, 33–68.

(24) Lauber, P.; Lu, Z. Analytical finite-Lamor-radius and finite-orbit-width model for the LIGKA code and its application to KGAM and shear Alfvén physics. *Journal of Physics: Conference Series* **2018**, *1125*, 012015.

(25) Artaud, J.; Imbeaux, F.; Garcia, J.; Giruzzi, G.; Aniel, T.; Basiuk, V.; Bécoulet, A.; Bourdelle, C.; Buravand, Y.; Decker, J. et al. Metis: a fast integrated tokamak modelling tool for scenario design. *Nuclear Fusion* **2018**, *58*, 105001.

(26) Pereverzev, G. V.; Yushmanov, P. N. *ASTRA. Automated System for Transport Analysis in a Tokamak*; 2002.

(27) Fitzgerald, M.; Sharapov, S.; Rodrigues, P.; Borba, D. Predictive nonlinear studies of TAE-induced alpha-particle transport in the Q = 10 ITER baseline scenario. *Nuclear Fusion* **2016**, *56*, 112010.

(28) Lauber, P. Local and global kinetic stability analysis of Alfvén eigenmodes in the 15 MA ITER scenario. *Plasma Physics and Controlled Fusion* **2015**, *57*, 054011.